



## RESEARCH ARTICLE

10.1002/2016JE005160

## Key Points:

- Both local and distal material transports by impacts play an important role in mixing across mare/highland contacts
- The variation in the abundance of exotic material in lunar mare soil hand samples can be accounted for by the patchy nature of crater rays
- Our result supports a Copernicus Crater provenance for ray material at the Apollo 12 landing site

## Correspondence to:

Y.-H. Huang,  
huang474@purdue.edu

## Citation:

Huang, Y.-H., D. A. Minton, M. Hirabayashi, J. R. Elliott, J. E. Richardson, C. I. Fassett, and N. E. B. Zellner (2017), Heterogeneous impact transport on the Moon, *J. Geophys. Res. Planets*, 122, 1158–1180, doi:10.1002/2016JE005160.

Received 19 AUG 2016

Accepted 24 APR 2017

Accepted article online 12 MAY 2017

Published online 3 JUN 2017

## Heterogeneous impact transport on the Moon

Ya-Huei Huang<sup>1</sup> , David A. Minton<sup>1</sup>, Masatoshi Hirabayashi<sup>1</sup> , Jacob R. Elliott<sup>1</sup> , James E. Richardson<sup>2</sup>, Caleb I. Fassett<sup>3,4</sup> , and Nicolle E. B. Zellner<sup>5</sup>

<sup>1</sup>Department of Earth, Atmospheric, and Planetary Sciences, Purdue University, West Lafayette, Indiana, USA, <sup>2</sup>Planetary Science Institute, Tucson, Arizona, USA, <sup>3</sup>Department of Astronomy, Mount Holyoke College, South Hadley, Massachusetts, USA, <sup>4</sup>Now at NASA Marshall Space Flight Center, Huntsville, Alabama, USA, <sup>5</sup>Department of Physics, Albion College, Albion, Michigan, USA

**Abstract** Impact cratering is the dominant process for transporting material on the Moon's surface. An impact transports both proximal material (continuous ejecta) locally and distal ejecta (crater rays) to much larger distances. Quantifying the relative importance of locally derived material versus distal material requires understandings of lunar regolith evolution and the mixing of materials across the lunar surface. The Moon has distinctive albedo units of darker mare basalt and brighter highland materials, and the contacts between these units are ideal settings to examine this question. Information on the amount of material transported across these contacts comes from both the sample collection and remote sensing data, though earlier interpretations of these observations are contradictory. The relatively narrow (~4–5 km wide) mixing zone at mare/highland contacts had been interpreted as consistent with most material having been locally derived from underneath mare plains. However, even far from these contacts where the mare is thick, highland material is abundant in some soil samples (>20%), requiring transport of highland material over great distances. Any model of impact transport on the Moon needs to be consistent with both the observed width of mare/highland contacts and the commonality of nonmare material in mare soil samples far from any contact. In this study, using a three-dimensional regolith transport model, we match these constraints and demonstrate that both local and distal material transports are important at the lunar surface. Furthermore, the nature of the distal material transport mechanism in discrete crater rays can result in substantial heterogeneity of surface materials.

## 1. Introduction

Impactors not only bombard the Moon but also initiate the transport of material across the Moon's surface. An impact excavates material from below the surface and emplaces it as a continuous ejecta blanket surrounding the crater and distal ejecta in rays at large distances. The proximal material in the continuous ejecta deposit is transported at low velocities and thus deposited locally. Most of the excavated mass is deposited locally. On the other hand, material originating in a region closer to the impact point can be thrown to much larger distances, forming secondary crater fields and crater rays [Shoemaker, 1965]. This distal ejecta is widely dispersed, relatively low in mass, and mixes more with preexisting material upon deposition [Oberbeck, 1975].

The first Apollo mare soil samples returned to Earth consisted of material of a variety of compositions, including both local mare basalts and more distantly sourced highland anorthosites [Wood, 1970; Wood *et al.*, 1970b, 1970a]. The anorthositic material in mare soil samples could either be derived from the underlying highland layer beneath mare surface or may have originated far from the sampling site [Arvidson *et al.*, 1975; Rhodes, 1977; Horz, 1978; McKay *et al.*, 1978; Labotka *et al.*, 1980; Laul and Papike, 1980; Simon *et al.*, 1981, 1990; Farrand, 1988; Fischer and Pieters, 1995]. The hypothesis that the source of anorthositic material in a mare soil came from beneath the mare deposit was favored until it came to be understood that the majority of mare plains are thick: up to kilometers at their center, decreasing to approximately hundred meters at the edges of the plains [De Hon, 1974; Horz, 1978; Head, 1982; Budney and Lucey, 1998; Evans *et al.*, 2016]. Only the largest postmare craters can excavate underlying highland materials, and the presence of a substantial anorthositic component in a mare soil samples must therefore originate from far away.

Material transport by impacts is an important process across all size scales. Small impacts constantly mix the uppermost layers of the lunar soil. Mixing of local materials leads to a well-mixed layer called the reworking zone [Gault *et al.*, 1974; Morris, 1978; McKay *et al.*, 1991]. For example, the Apollo 15 deep drilling core has been interpreted as having ~242 well-mixed layers with thicknesses between a few millimeters and

©2017. The Authors.

This is an open access article under the terms of the Creative Commons Attribution-NonCommercial-NoDerivs License, which permits use and distribution in any medium, provided the original work is properly cited, the use is non-commercial and no modifications or adaptations are made.

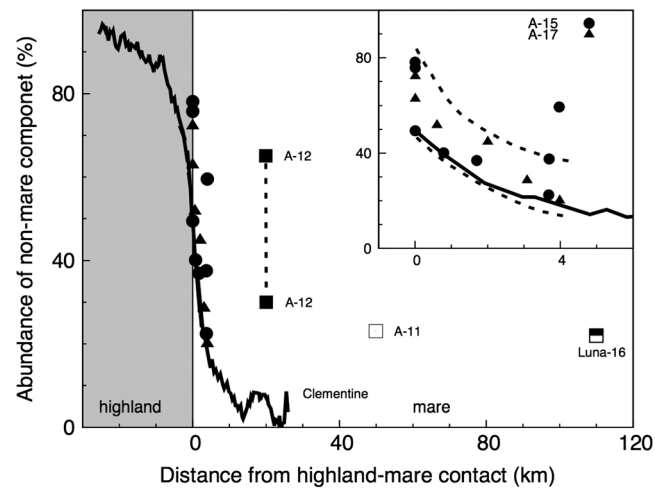


**Figure 1.** Abundance of nonmare material as a function of sampling distance from the highland and mare contact as measured by Clementine, Apollo, and Luna missions. This plot is modified from Figure 1 in Rhodes [1977], with the addition of Clementine UV/VIS camera data for Grimaldi Crater (solid line) that is directly taken from Li and Mustard [2000]. The vertical line at zero distance in the x axis is the geological contact between anorthositic highlands on the left-hand side (shadowed in gray color) and mare on the right-hand side. The Apollo 11, 12, 15, and 17 and Luna 16 data are hand samples assembled by Rhodes [1977]. Apollo 15 and 16 samples are compared with Clementine data for all four contacts in greater detail in the inset.

basalts, this mixing zone was a very narrow and sharp contact existed between the mare and highland plains. If local material transport dominates, then an insignificant amount of material would be transported across the contact, so the expectation is that boundaries would remain relatively sharp. On the other hand, if distal ejecta dominates, one would expect a wider mixing zone. The Apollo and Luna sample sites were located at a wide range of distances from mare/highlands boundaries, allowing us to see how the basalt/anorthosite mixing ratio varies with distance.

The mare soil samples of Apollo 15/17, Apollo 12, Apollo 11, and Luna 16 were taken at less than 0–4 km, ~20 km, ~50 km, and ~110 km from their nearest mare/highland boundary, respectively. When we examine the basaltic/anorthositic mixing ratio with each sampling distance, it appears that the samples collected further away from the nearest contacts are not as strongly correlated to sampling distance as the samples collected at a much closer distance. The amount of nonmare material in Apollo 11, Apollo 12, and Luna 16 mare soil samples, which extend up to 100 km from the nearest highland contact, is about 20% on average, with the exception of a few Apollo 12 samples, which are ~20 km from the highlands and reach nonmare fractions of up to 70% (Figure 1) [Wood, 1970; Goles et al., 1971; Hubbard et al., 1971; Schnetzler and Philpotts, 1971; Schonfeld and Meyer, 1972; Wanke et al., 1972]. The elevated abundance of nonmare material found in most mare soil samples at these large distances would suggest their origin as distal ejecta.

In contrast, the Apollo 15 and 17 missions were near the edge of the maria and close to the contact with highlands. The astronauts collected samples at varying distances but all within 4 km of the contact [NASA Technical Report Server, 1972, 1973]. The amount of highland material in mare soils sampled by both missions decreased rapidly with distance from the contact (Figure 1). The narrow mixing zones observed in these near-contact sampling sites are suggestive of a different trend in exotic material abundance as a function of distance compared to the more distant Apollo 11 and 12 and Luna 16 samples. The observations of an active reworking zone and narrow mixing zones seen at the Apollo 15 and 17 sites imply that a proximal ejecta-dominated local mixing process is most important, while the amount of nonmare material in the more distant mare soils implies distal ejecta-dominated mixing [Shoemaker, 1970; Wasson and Baedeker, 1972; Oberbeck et al., 1973; Gault et al., 1974; Rhodes, 1977; Horz, 1978]. This discrepancy has remained unresolved.

~13 cm [Taylor, 1982]. Additionally, the transport of material by impacts is apparent in the Apollo 14 impact glasses [e.g., Zellner et al., 2002]. For example, impact glasses with feldspathic compositions are abundant even though the typical Apollo 14 regolith is mostly potassium, rare earth element, and phosphorus (KREEPy). It remains unclear, however, how much proximal ejecta versus distal ejecta contributes to the make-up of lunar regolith.

One way to evaluate the relative importance of proximal ejecta and distal ejecta is to examine how the basalt/anorthosite material mixing ratio changes as a function of distance from a mare/highland boundary [Schonfeld and Meyer, 1972; Rhodes et al., 1974; Rhodes, 1977; Li et al., 1997; Li and Mustard, 2000]. The material mixing process across mare/highland contacts is driven by impacts, and the area where this mixing occurs is called the mixing zone. Immediately following the eruption and emplacement of the mare

The impact transport process can be further constrained using remote sensing observations. The Clementine UV/VIS (ultraviolet/visible) camera obtained ~120–170 m/pixel resolution multispectral reflectance data for the Moon [Nozette *et al.*, 1994]. Because of the albedo contrast between darker basaltic mare and brighter anorthositic highlands, Li and Mustard [2000] used this Clementine reflectance data to quantitatively estimate how much material has been transported across mare/highland contacts for four basins. The UV/VIS imaging data revealed a sharp decrease in the abundance of foreign material, dropping from ~50% at the contact to ~10–30% at ~4–5 km from the contact (see inset of Figure 1). This analysis is consistent with the in situ sampling results of the Apollo 15 and 17 missions, both of which are highly correlated with sampling distance from the contact. Thus, the narrow mixing zones seen in both the Apollo 15 and 17 sampling and Clementine data seem to support the hypothesis that local material dominates at the lunar surface.

If locally derived materials dominate on the lunar surface, and distal ejecta is insignificant, then the mixing process across mare/highland contacts can be modeled by only considering deposition of the proximal continuous ejecta. Li *et al.* [1997] modeled the material exchange between mare and highland plains as a classical diffusion process, which describes the movement of a particle as random walk, with each step of motion spanning a finite distance. The finite step that a crater generates is limited to the extent of the continuous ejecta blanket. However, the classical diffusion model results in an even narrower mixing zone (<1 km) than is observed, which conflicts with both the Clementine and Apollo 15 and 17 results. Thus, Li *et al.* [1997] concluded that local material transport could not be the dominant mixing process at mare/highland contacts. Therefore, some amount of distal ejecta must play an important role in transporting material across mare/highland contacts.

Instead of the classical diffusion model, Li and Mustard [2000] used an anomalous diffusion model in which the movement step is not limited to the extent of the continuous ejecta blanket but can be larger or even infinite. The anomalous model is more realistic because large craters deposit material far from their source region. Their anomalous diffusion model successfully reproduced the 4–5 km wide mixing zone seen in the Clementine data. They suggested that distal ejecta is what determines the width of this narrow mixing zone. With some simplifying assumptions, such as that the ejecta was radially homogeneous and followed a simple power law thickness profile that extended to infinite distance, Li and Mustard [2000] were able to reveal the relative importance of proximal (local) ejecta and distal ejecta on the Moon. Yet this result is still at odds with the observed elevated abundances of exotic material seen in the Apollo 11 and 12 and Luna 16 samples that are much farther away from the source of highland material.

Here we propose a new model that accounts for the spatially heterogeneous nature of distal ejecta. The ejecta are only continuous to ~2–3 radii distance, and beyond that, they break into discontinuous rays [Howard, 1974]. By accounting for this nature of the ejecta, we investigate both the 4–5 km wide mixing zone across contacts and the elevated nonmare abundances at further distances. We model the impact-driven material transport and mixing processes across mare/highland contacts with a fully three-dimensional regolith tracking code. Our code includes treatments of the reworking zone of locally derived material, as well as both continuous proximal and discontinuous distal ejecta (crater rays). This material transport and mixing code is built on top of a Monte Carlo terrain evolution code called the Cratered Terrain Evolution Model (CTEM) [Richardson, 2009; Minton *et al.*, 2015]. In section 2 we discuss the observational constraints on transport of material by impacts in detail. In section 3 we discuss how we developed our new three-dimensional material transport and mixing code. This section is a highly detailed technical explanation of the models we have incorporated into the CTEM code. Readers interested in the results of our study may wish to skip section 3 and read the results in the sections that follow, and we have written the result sections (sections 4–6) with this in mind.

In section 4 we apply our new code to the problem of material transport across the mare and highland boundary of Grimaldi Crater. In section 5 we discuss how discontinuous distal ejecta may explain the discrepancy between the wide mixing zone implied by the Apollo 11 and 12 and Luna 16 samples and the narrower mixing zone implied by the Apollo 15 and 17 samples and Clementine remote sensing observations. Finally, in section 6 we use our simulation results to discuss the implications of the heterogeneous nature of distal ejecta.

## 2. Two Sets of Contradictory Observational Constraints on Material Transport

In our study, we wish to understand what processes are responsible for transporting and mixing material at the lunar surface. We will use two data sets that will constrain the material fraction as a function of distance from a highland/mare contact. These data sets are distinguished by their sampling distance from the nearest mare/highland contact. The first data set includes Apollo 12 and 11 and Luna 16 soil samples, which are sampled at large distances from the contact: 20, 50, 110 km, respectively. Wood [1970] classified 1676 lithic fragments in the 1–5 mm size range from 11.1 g of the Apollo 11 coarse fines (sample (10085,24) with sizes >1 mm). The visible anorthositic fragment (5%) and some anorthositic component embedded in basalt breccia amount to 20% in their Apollo 11 soil sample. The chemical mixing model of *Schonfeld and Meyer* [1972] also showed the Luna 16 soil has 20% anorthositic gabbro and 2% KREEP as representative of nonmare components. Intensive compositional analysis on Apollo 12 soil samples presents a mixture of up to 30–70% KREEP material and basalt [Goles *et al.*, 1971; Hubbard *et al.*, 1971; Schnetzler and Philpotts, 1971; Wanke *et al.*, 1972]. These mare soil samples show >20% anorthositic material, with some Apollo 12 samples reaching up to 70% (Figure 1). Later, the Apollo 15 and 16 orbital X-ray experiments created compositional maps of several mare surfaces (e.g., Mare Imbrium and Mare Serenitatis). The compositional maps closely match the soil samples, with elevated levels of aluminous or anorthositic material [Trombka *et al.*, 1974]. The more anorthositic mare surfaces indicate that distal materials from the highlands contaminate the mare surfaces.

The second data set consists of Apollo 15 and 17 mare soil samples and Clementine remote sensing data sets that sampled the spectral reflectances of Mares Grimaldi, Tsiolkovsky, Orientale, and Fecunditatis from mare/highland contacts at a short distance (4–5 km). Rhodes [1977] assembled component estimates of those Apollo 15 and 17 mare soil sample from three studies of *Schonfeld and Meyer* [1972], Rhodes *et al.* [1974], and Duncan *et al.* [1975]. The inset of Figure 1 shows the strong correlation between nonmare abundance and distance. Although the abundances of the anorthositic component in the Apollo 15 and 17 mare soil samples appear to vary by location, they still show a decrease from 50–80% at the mare/highland contact to 20–40% at the edge of the mixing zone. Despite the compositional variability seen in the Apollo 15 and 17 samples, Clementine UV/VIS data sets for all four basins fall within the range of the samples, except for Mare Tsiolkovsky, whose mixing zone is narrower than that of each of the other three basins. Both Clementine UV/VIS data sets and Apollo 15/17 mare soil samples are consistent with each other, although the Apollo 15 and 17 mare soil samples were taken only on the mare side and only within 4 km of the mare/highland contact. The Clementine data sets cover a much larger distance and contain observations from both the mare and highland side of the boundaries. The Clementine data suggest <10% exotic material at a distance of 20 km from the boundary, while the Apollo 11 and 12 and Luna 16 mare soil samples are composed of >20% nonmare component at further distances.

As crater rays commonly cross mare surfaces, they may deliver anorthositic material from highland regions. For example, the ray material from Theophilus Crater (100 km in diameter), which is ~8 crater radii away from the Apollo 11 landing site, may be a significant contributor to the highland component of the Apollo 11 samples [Pieters *et al.*, 1985; Hawke *et al.*, 1999]. Similarly, the ejecta from Copernicus Crater (96 km in diameter), which is ~8–9 radii from the Apollo 12 and 14 landing sites, could contribute a large portion of the material in the samples collected at those sites [Pieters *et al.*, 1985]. The Copernicus ejecta are potentially sourced from the highland-like layers beneath the mare plain. As a result, the Apollo 12 landing site, which is crossed by a ray of Copernicus Crater, could have higher abundances of anorthositic materials than other nearby mare plains. In addition, rays from either Autolycus or Aristarchus Crater are seen crossing the Apollo 15 landing site area [Carr *et al.*, 1971].

We propose a hypothesis that could account for the discrepancy between the inferred widths of the mixing zones seen in the different data sets. We suggest that because distal impact ejecta are concentrated into thin rays, there is large spatial variability, on small spatial scales, in the abundance of nonlocal material. Therefore, samples from the surface should show greater variability in nonlocal abundance compared to remote sensing observations, which average out the spatial heterogeneities. For example, the Apollo 15 lunar module site was in the secondary field (South Cluster) of rays of either Autolycus or Aristarchus Crater [Swann *et al.*, 1972]. Li and Mustard [2005] suggest that distal ejecta from distances of >100 km away could explain an elevated amount of nonlocal material in a sampling location, though, again, they did not consider the heterogeneous nature of this distal ejecta.

The above demonstrates a need for a material-transport model that takes into account the spatial heterogeneity due to crater ray emplacement. In the next section, we will discuss our three-dimensional regolith transport model that includes four components. The first component is an efficient approximation to the excavation flow within a transient crater that is based on the Maxwell Z model [Maxwell and Seifert, 1974; Maxwell, 1977]. This component of our model allows us to model the mixture of material that is incorporated into ejecta during the excavation process. The second component is an empirically derived geometric model for crater rays. This component allows us to model the spatial heterogeneity of distal ejecta deposits. The third component is a mixing component that allows us to model the local zone reworked by those craters that are smaller than our code can directly resolve. The last component is also a mixing component but reworking local materials by the deposition of crater ray ejecta.

### 3. A Three-Dimensional Regolith Transport Model

Our three-dimensional regolith transport model is based on the CTEM Monte Carlo cratering code [Richardson, 2009; Minton *et al.*, 2015]. We have modified CTEM to study the transport of materials by impacts across the mare/highland contact. CTEM was originally designed to study how impact cratering shapes the topography planetary surface and tracks the number of countable craters over time. A planetary surface in CTEM is modeled as a discrete grid of square cells that each represents a portion of the planetary surface. The square grid of cells possesses periodic boundary conditions so that the grid represents a single contiguous surface. In this way, craters and their ejecta are simulated smoothly across the domain boundary. As CTEM copes with multiple cratering events in a single simulation, each crater is generated from parameterized models that draw an impactor size, velocity, and impact angle from appropriate probability distributions. Using the chosen impactor parameters, CTEM creates a crater whose morphology is determined using appropriate crater scaling relationships. The size of each crater is determined based on the Pi-group scaling laws [Holsapple, 1993].

For our study, we chose a model impactor population, velocity distribution, and set of scaling law parameters such that the resulting crater size-frequency distribution matches the Neukum Production Function (NPF) [Neukum *et al.*, 2001]. After the generation of a crater and its ejecta, the surface elevation is modified in accordance with deposition of an ejecta and excavation of a crater. CTEM also takes into account the elevation changes caused by degradation processes, such as sandblasting by small impacts and unstable slope collapse. Each grid cell of CTEM stores the information of surface elevation and ejecta accumulation. We modified the code so that ejecta accumulation includes not only the thickness but also the composition of a parcel of ejecta. We use a two component material model that represents the relative abundance in each ejecta parcel of either mare basalt or highland anorthosite.

We briefly introduce the discussions in the following sections. The volume of material that is transported across contacts is critical, and in section 3.1, we describe how CTEM calculates each crater's ejecta volume and how we can use the concept of streamlines (Maxwell Z model) to estimate the mixture of our two material components found in each crater's ejecta parcels. In section 3.2, we use a simple mathematical formula to represent the radial distribution of distal ejecta that mimics lunar crater rays. Finally, section 3.3 describes our model for material mixing by craters that are smaller than the grid cell resolution that we use to model mixing by both subpixel primary craters and distal rays of larger craters.

#### 3.1. The Dynamic Stream Tube-Based Transport Model

For our simulations of the mare and highland contact, the CTEM grid space is split in half, where one half contains a layer of mare basalt 4 km thick on top of a highland anorthosite layer and another half is purely highlands anorthosite (Figure 2). Figure 2 illustrates a schematic of the cross section of our modeled mare and highland contact both near the beginning of the simulation and later as the simulation has progressed and impacts have redistributed material around the domain. To model the transportation process, the ejecta from each impact must be traced back to its source location within the transient crater in order to calculate its unique compositional mixture. CTEM contains a paraboloid shell model that computes the thickness of the ejecta as a function of distance from the impact site, and we continue to use this method for the total ejecta thickness calculation [Richardson, 2009].

However, our task is somewhat more complex. We must be able to quickly determine the fraction of mare and highland material that is entrained in the excavation flow that makes up each parcel of ejecta. A

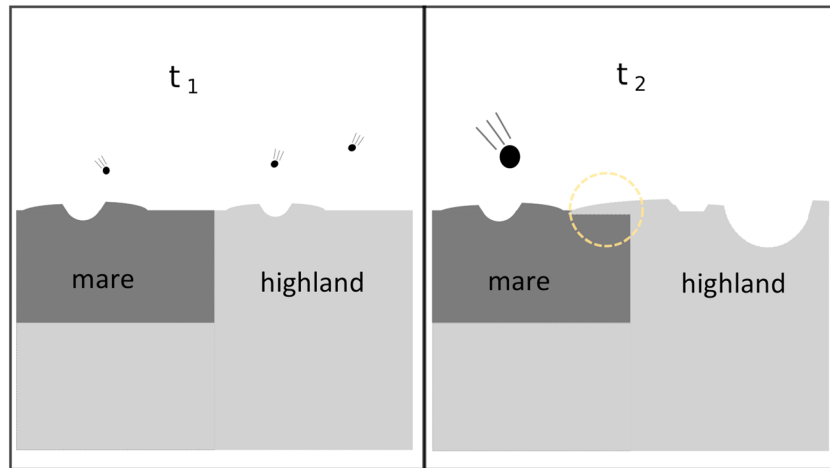


**Figure 2.** A schematic of cross section of modeled mare and highland contact in CTEM. The mare side with a finite thickness is marked as dark gray color, and the highland side is light gray color. The left-hand side figure shows the beginning of an impact cratering process across the contact ( $t_1$ ), and the right-hand side represents a scenario of large crater showing up at  $t_2 > t_1$ . Note that a large crater on the highland side is able to deliver highland material to mare side (dashed circle in yellow color).

parcel of ejecta in CTEM is a cuboid of material that occupies a single grid cell with a height determined by the paraboloid shell-based ejecta thickness calculation from Richardson [2009]. To determine the amount of mare and highland material of a parcel of ejecta during excavation, we need to know the makeup of material that was intersected by the streamlines that made up the excavation flow of each ejecta parcel. As regolith is reworked, the composition of any given grid cell will take on a very complex layered structure. By overlying each ejecta parcel's streamlines onto the preexisting compositional layers at the site of the excavation, we can estimate the new composition of each ejecta parcel.

The relationship between radial distance of an ejecta and its ejection velocity or launching velocity is key to ejecta emplacement in CTEM. Richardson *et al.* [2007] used crater ejecta scaling laws derived from the work of Housen *et al.* [1983]. CTEM traces the ejecta to the transient crater and uses the paraboloid shell to approximate the total volume of ejecta in any direction at the distance. The thickness of ejecta at this distance is averaged over the landed area [see Richardson, 2009, equations (25)–(27)]. Because the geometry of the true excavation flow is different than a paraboloid shell, this technique is inaccurate when attempting to map the provenance of ejecta back to the excavation flow volume. We therefore will use a hybrid approach, where the ejecta thickness is obtained by a simple empirically derived power law function, but the compositional ratio of ejecta is determined using the Maxwell Z model.

To model the bulk composition of the material within each parcel of ejecta, we make use of the Maxwell Z model. In the Maxwell Z model, excavated materials from a transient cavity are treated as an incompressible fluid [Maxwell and Seifert, 1974; Maxwell, 1977]. The flow of excavated material within a transient crater is often formulated as streamlines in polar coordinates (Figure 3),

$$r(\theta) = r_0(1 - \cos\theta)^{\frac{1}{Z-2}}, \tag{1}$$

where  $Z$  determines the shape of a streamline ( $Z = 3$  in our model),  $r_0$  is the radial distance from the center of the impact site to location at which the streamline emerged from the free surface,  $r(\theta)$  is the radial distance from the center of the impact site to the current location of a streamline within a transient crater, and  $\theta$  is the polar angle measured from the local vertical. At the emerging location,  $\theta = 90^\circ$ . Note that the choice of  $Z = 3$  in this study is the simplest (and analytically solved) for implementation. A lower value of  $Z$  (e.g., 2.7) would be a better choice, yet  $Z = 3$  is overall reasonable for approximating the crater excavation stage [Melosh, 1989].

Figure 3 shows that streamlines closer to the impact point are faster resulting in distal ejecta, while continuous ejecta blanket mostly comes from streamlines closer to the edge of a transient cavity. Each ejecta parcel is bounded by four corners of a square grid cell. As a result, the ejecta is created by a stream tube with a highly distorted quadrilateral cross section. The distortion of the quadrilateral cross section is due to a

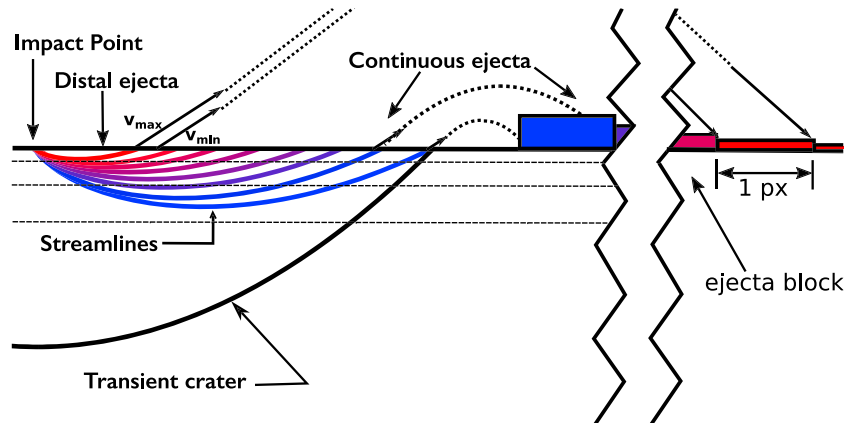


**Figure 3.** The provenance of an ejecta parcel within a transient crater. Streamlines within a transient crater are highlighted in red and blue colors. The redder the color of a streamline, the faster the ejection speed of a streamline. The magnitude of ejection speed of a streamline is represented by the length of arrow in black color. The length of arrow is arbitrary, but it gives a sense of that the closer to the impact point, the faster a streamline. Slower streamlines deposit as closer to the crater (continuous ejecta), and faster streamlines land at large distances (distal ejecta). A single block of ejecta occupying a single grid cell (pixel) is highlighted in red or blue, depending on the speed of streamlines. The volume of the ejecta block is determined by the volume of material bounded by the streamlines that exit with velocities  $v_{min} < v < v_{max}$ , which define a stream tube. The horizontal dotted lines denote notional layers of compositionally distinct material. The final composition of the ejecta block is determined by the mixture of material contained within the stream tube.

difference in the ejection velocities for each corner of the square grid cell corresponding to each ejecta parcel. Calculating the exact shape of this highly distorted stream tube is computationally expensive and impractical to do in CTEM.

However, our goal is not to accurately model each stream tube, but to quickly estimate the mixing ratio of material along the stream tube's path. We therefore approximate each stream tube as having a circular cross section, with the total volume determined using the paraboloid shell approximation. Figure 4 shows a schematic of our three-dimensional circular stream tube with its corresponding landing distance. We characterize our three-dimensional stream tube with two parameters: the radius of a circle at the emerging location ( $\delta r$ ) and the radial distance from the emerging location to the impact site ( $r_0$ ) as shown in Figure 4b. In the following paragraphs we first introduced an analytical equation of a stream tube's volume then described a stream tube residing in a layer system based on linked list structure, which allows us to gain the information of depth for a given pixel.

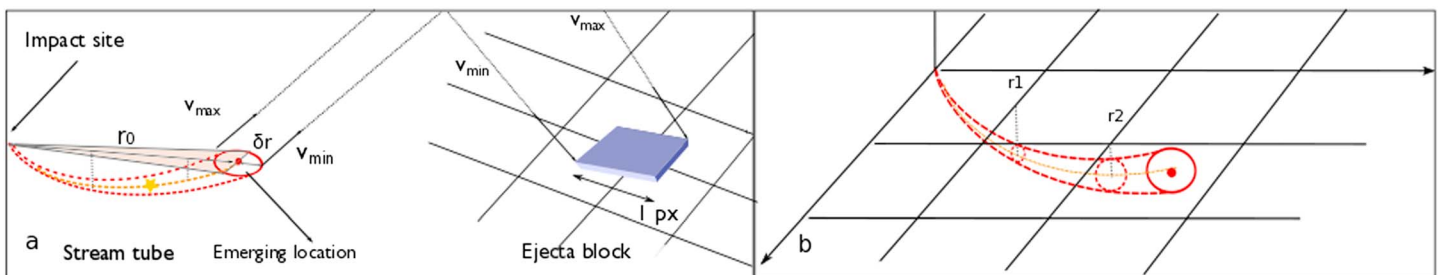


**Figure 4.** A schematic of a three-dimensional circular stream tube. (a) Stream tube in side view as well as its corresponding ejecta deposit. A stream tube is characterized by a circular section of radius ( $\delta r$ ) of a stream tube at the emerging location and radial distance from the impact site to the emerging location ( $r_0$ ). The red dot in the center of the stream tube is the emerging location. The solid line outlined triangle filled with light orange color is the projection area of a stream tube on the surface. The centerline inside the triangle represents a projection of an axis of a stream tube (dashed line in orange color). (b) Stream tube within the grid space of CTEM. The intersection points between the centerline of a stream tube on the surface and the grid lines are labeled by  $r_1$  and  $r_2$ , which characterize a segment of a stream tube within a pixel space. The dashed lines represent that a stream tube is under the surface. The vertical and dotted lines in gray color at the intersection points attempt to guide readers to the interface of a stream tube with the virtual grid underneath, which are circles outlined in dashed line and red color. The star filled in yellow color is the intersection point that a segment of a stream tube encounters a layer under surface.

First of all, given the circular cross section of a stream tube, one can integrate the volume along the direction of radial distance even though the radius of a circular cross section varies along the stream tube. The total volume of our circular stream tube,  $V_{st}$ , is given as

$$V_{st} = \int_0^{\theta_0} \pi(\delta r(r(\theta)))^2 dr, \quad (2)$$

where  $r(\theta)$  is the radial distance at a given polar angle measured from local vertical and  $\delta r(r(\theta))$  is the radius of a cross section at a given radial distance from the impact site. Here the volume of a stream tube and the integration range (radial distance) can be obtained from CTEM. The relationship between the radius of a cross section and its radial position along the stream tube is the only unknown. This relationship is independent of crater size and can be described by a tangential function,

$$\delta r(r(\theta)) \propto \frac{a}{r_0} \tan \left[ \frac{b}{r_0} r(\theta) \right], \quad (3)$$

where  $a$  and  $b$  are fitting parameters for all stream tubes within a transient crater for a given size. We find these to be  $a \approx 0.936457$  and  $b \approx 1.12368$ , respectively. Then, by integrating this scaling relationship along the stream tube, an analytical function for the volume as a function of radius,  $\delta r$ , and radial position,  $r$ , is given as

$$V_{st}(\delta r, r_0) = \frac{1}{4} \pi (\delta r)^2 a^2 \frac{r_0}{b} [\tan(b) - b] + \frac{\pi}{\sqrt{2}} (\delta r)^3. \quad (4)$$

Equation (4) only leaves  $\delta r$  unknown. For a given volume of a stream tube, the variable of  $\delta r$  in equation (4) can be solved. The total volume of an ejecta ( $V_{st}(\delta r, r_0)$ ) for a given pixel is expressed by  $A_{\text{pixel}} \times t_e$ , where  $A_{\text{pixel}}$  is the area of a pixel and  $t_e$  is the thickness of the ejecta parcel as determined using the paraboloid shell model used in CTEM [Richardson, 2009].

We next need to know the makeup of preexisting material of the stream tube. We first identify all pixels that overlap with a stream tube by projecting the axis of a stream tube onto the surface (see Figure 4a). Each of these pixels will have one or more layers that intersect a stream tube at some depth, and we need to calculate the volume of intersection between the stream tube and these layers. Before we consider each layer, we first calculate the volume of intersection between the stream tube and the total column of material beneath each pixel it intersects. The segment of a stream tube starts from the radial distance of  $r_1$  to the radial distance of  $r_2$  relative to the center of a crater (see Figure 4a). By using equation (4), the volume of intersection between the stream tube segment and the pixel is the subtraction between  $V_{st}(\delta r, r_1)$  and  $V_{st}(\delta r, r_2)$ . It can be analytically expressed in equation (5),

$$V_{\text{seg}} = \frac{1}{4} \pi (\delta r)^2 a^2 \frac{r_0}{b} \left\{ \left[ \tan \left( \frac{b}{r_0} r_2 \right) - \frac{b}{r_0} r_2 \right] - \left[ \tan \left( \frac{b}{r_0} r_1 \right) - \frac{b}{r_0} r_1 \right] \right\}; r_2 > r_1, \quad (5)$$

where  $V_{\text{seg}}$  is the volume of a segment with the length of  $r_2 - r_1$  within a pixel. As a result, a stream tube can be dissected into one or more than one segments depending on the location of a stream tube within a transient crater and the size of a pixel in CTEM. We expect some minor error in the estimate of a segment's volume because for expediency, we only locate pixels that overlap along the center line of a stream tube. From a practical standpoint, we find that most stream tubes are narrow and confined within a pixel along the path.

Using equation (5), we can quickly estimate the volume fraction of material entrained along the excavation flow of each parcel of ejecta. Each parcel of ejecta is tracked as a compositionally distinct layer and is emplaced on the top of any preexisting layers. As subsequent craters may excavate one or more than one of those compositionally distinct pixels, recording all deposits from each cratering event is mandatory for this study. For our current problem, each ejecta block is tracked with a single number that stores the mare fraction: 0 equals pure highlands and 1 equals pure mare.

To keep track of each distinct ejecta layer from a cratering event over time, we use a dynamic data structure called a linked list to record every ejecta block as a distinct layer at each grid cell. This dynamic data structure has more flexibility than a fixed array, as the number of layers can be redefined on the fly using two main operations (executed in a first in/last out manner). When an ejecta block is deposited in a given grid cell, a "push" operation is executed, basically adding a new layer of specified thickness and mixing ratio on the

top of the surface at that location. If a grid cell experiences an excavating event, such as within a transient crater, for example, a “pop” operation is executed, and a layer, or several layers depending on the excavation depth, will be removed from that location. Each grid cell location records a compositionally unique layered structure as a result of impact excavation and deposition.

To obtain the amount of mare and highland material of each ejecta parcel, we need to estimate the intersected volume between a segment of a stream tube and a layer. Figure 4b shows how a segment of a stream tube looks like under a surface. We traced the centerline of a stream tube in a layer structure and projected the intersection point to the surface for obtaining the radial distance so that the volume between neighboring intersection points can be calculated by equation (5). Continue to the example of Figure 4a, if this segment with the length of  $r_2 - r_1$  is sitting between two layers, we can obtain the location of an intersection point between the depth of the first layer and the centerline of a segment (see yellow star in Figure 4a). Assuming that each of these two layer contains a mare fraction,  $f_1$  and  $f_2$ , the final mare fraction of a segment is the total mare volume normalized by the total volume of the segment,

$$f_{\text{seg}} = \frac{f_1 \times V_{\text{seg}}^1 + f_2 \times V_{\text{seg}}^2}{V_{\text{seg}}}, \quad (6)$$

where  $V_{\text{seg}}^1$  and  $V_{\text{seg}}^2$  are the volume of a segment intersected with the first and second layers, respectively.

Here we illustrate a calculation of mare fraction for a segment of a stream tube for an example of a two-layer structure. As more ejecta layers build up over time, a segment of a stream tube may overlap with several layers. Note that the approximated volume of a segment with a layer is not aligned up with horizontal layer but perpendicular to the layer. However, we confirm that our estimates are efficient and only have some small difference from exact volume. The total volume of both materials is conserved over the course of a single full simulation. Finally, CTEM loops over all pixels that a stream tube superposes, and the calculation of a mare fraction for a whole stream tube follows the same manner.

### 3.2. An Empirical Model for the Spatial Geometry of Crater Rays

In observed lunar craters, the continuous ejecta blanket usually extends to 2–3 radii from the center of the crater. Beyond this range, the ejecta breaks up into discontinuous structures in the form of crater rays and secondary craters. The anomalous diffusion model of *Li and Mustard* [2000] did not take into account the discontinuous nature of distal ejecta but instead modeled each crater as having an infinite continuous ejecta blanket. The Lunar Reconnaissance Orbiter Camera (LROC) instrument (50 cm/pixel) has imaged fresh crater rays [*Robinson et al.*, 2010], which display the nearly pristine original ejecta pattern of a fresh crater. Initial crater ray material may be brighter than surrounding background material, but cosmic rays, solar wind, or micrometeoroids weather that bright material, resulting in a decrease in their albedo over time until they are no longer distinguishable from the surrounding lunar background. Most craters have no visible rays, which is accounted for by their long exposure time on the lunar surface.

*Elliott et al.* [2016] mapped lunar rayed craters and performed a systematic study of the distribution of their morphology, length, number, and width. In general, ray morphology is divided into two types: flowery rays and spike-like rays. Flowery rays exhibit feathered boundaries that often overlap with neighboring flowery rays. Spike-like rays show a sharp boundary between rays and surroundings and are commonly observed in large or fresh craters. These two types of crater rays are usually found together in a single crater. For some craters those flowery rays are shorter than spike-like rays. Some craters may be dominated by one of these two patterns. For example, the ray system of Copernicus Crater is dominated by flowery rays. The ray morphology data of *Elliott et al.* [2016] suggest that the number of spike-like rays ranges from 6 to 14 per crater. The average length of flowery rays is about 5 to 7.5 crater radii, and the average length of the observable spike-like rays ranges from 5 to 55 crater radii.

Ray length highly depends on the efficiency of transport of distal ejecta. *Baldwin* [1963] reported that the average length of a crater’s observable rays ( $R_{\text{ray}}$ ) follows a power law function of crater radius ( $R_{\text{crat}}$ ) given by

$$R_{\text{ray}} = 10.5 R_{\text{crat}}^{1.25}. \quad (7)$$

*Elliott et al.* [2016] found that the end of rays may be determined by the point where the primary crater ejecta have become too small to overturn space-weathered “skin” that exists on the lunar surface [*Borg et al.*, 1976].

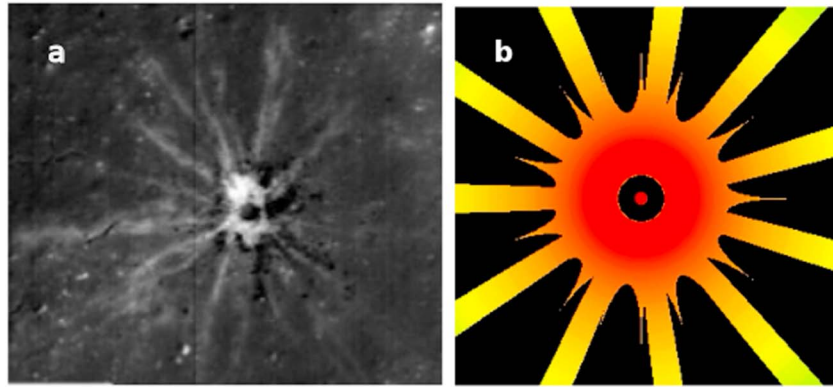


**Figure 5.** Comparison between an actual rayed crater and a model rayed crater. (a) Example of a fresh crater (LROC stamp: M1136364148RE) with a radius of ~6 m in radius. (b) Regolith map of a crater with our crater ray model. The crater is 0.146 km in diameter at 10 m/pixel resolution. The flowery rays surrounding the continuous ejecta extend to 7 radii from the crater’s center, and the spike rays extends outward until the regolith thickness reaches the cutoff value of  $10^{-8}$  m (not shown here). The variation in color represents the thickness of regolith (ejecta), ranging from none (black) to maximum (red).

This hypothesis suggests that the measured length of crater rays is likely shorter than the true length because the ejecta material becomes too small to affect the surface enough to be seen. *Li and Mustard* [2000] reproduced the width of the mare/highland mixing zone from Clementine UV/VIS data, assuming an infinite extent of distal ejecta in their mathematical model. Therefore, we assume that a crater ray could potentially reach farther than we observe them, but for numerical expediency, our crater ray extends until its vertical thickness reaches  $10^{-8}$  m, which is an order of magnitude smaller than the penetration depth of the UV/VIS wavelength region measured by Clementine.

We currently model ejecta blankets and rays as symmetrical, although we know that oblique impacts have an asymmetric ejecta distribution [*Moore and Baldwin, 1968; Howard and Wilshire, 1973; Gault and Wedekind, 1978*]. We assume that the effects of oblique impact angles are averaged out over a large number of cratering events. Using an empirically derived number and length of rays based on the mapping data of *Elliott et al.* [2016], we use a function called the Superformula by *Gielis* [2003] to approximate the spatial geometry of rays on the lunar surface. This formula can reproduce a wide variety of morphologies found in nature, ranging from basic shapes (circle, square, ellipse, and rose curve) to biological shapes (starfish, marine diatom, and flowers). It is not meant to model any kind of physical process that gives rise to crater rays, but rather to approximately mimic ray morphology and allow us to model the spatial heterogeneity of distal ejecta in a way constrained from observations of ray morphology.

The Superformula in polar coordinates is defined as

$$r(\phi) = \left\{ \left[ \left| \frac{1}{a} \cos\left(\frac{m}{4} \phi\right) \right|^{n_2} + \left| \frac{1}{b} \sin\left(\frac{m}{4} \phi\right) \right|^{n_3} \right]^{\frac{1}{n_1}} \right\}^{-1}, \quad (8)$$

in which the six parameters:  $a$ ,  $b$ ,  $m$ ,  $n_1$ ,  $n_2$ , and  $n_3$ , control shape (see detail below);  $\phi$  is polar angle ranging from 0 to  $2\pi$ ; and  $r(\phi)$  is the radius or distance from a point in polar coordinates to the origin of coordinates and can be expressed as  $\sqrt{x^2 + y^2}$  in Cartesian coordinates. In general,  $a$  is always equal to  $b$  for symmetric shapes. We used a specific parameter set for both spike-like and flowery rays in CTEM and superpose them to generate the complete ray geometry. The superposition of the Superformula equations that we developed for both ray patterns outlines the contour of rays (Figure 5).

The parameter of  $m$  determines the number of rays. For spike-like rays, it ranges from 6 to 14 per crater, and as a result, the values of  $m$  within the range of 6 and 14 with the exact number of any particular crater are determined using a random number generator. For flowery rays, we use 20 for the values of  $m$  parameter. The parameter of  $n_1$  controls the shape. We use 4.0 for spike-like rays and 1.0 for flowery rays. The parameters of  $n_2$  and  $n_3$  have an equal value, but their values depend on the length of the ray. By equaling the  $r(\phi)$  of the

Superformula in equation (8) to a desired ray length, we are able to derive a relationship between the value of  $n_2$  ( $n_3$ ) and a desired ray length,

$$n_2 = n_3 = 8 \times \left[ \log_{10} \left( 0.5 \times \frac{r_{\text{ray}}}{r_{\text{CE}}} \right) \right] + 2, \quad (9)$$

where  $r_{\text{ray}}$  can be the length of either spike-like rays or flowery rays, in which default length of spike-like ray is set 100 times longer than the extent of continuous ejecta blanket,  $r_{\text{CE}}$ . The output of shape of our crater rays is shown in Figure 5b.

The Superformula gives the spatial geometry of the ray, but we must also adjust the ejecta thickness within the ray to account for the inhomogeneity of the distal ejecta. In the distal ejecta regime in our model, only the rays contain ejecta mass. To conserve the total mass of ejecta in the distal rays, we calculate the areal fraction that is covered by ray material at any given landing distance,  $f(r)$ . The ejecta thickness inside a ray at a given landing distance ( $t_e'$ ) is then modified from an equivalent thickness ( $t_e$ ) if the ejecta were continuous by  $t_e' = t_e/f(r)$ . The ejecta thickness outside a ray is zero. In other words, at any given radial distance in the distal ejecta region, the amount of ejecta volume contained in rays is equal to the total volume of the excavation flow at the launching point corresponding to that distance, just as it is in the continuous ejecta blanket. This makes the ejecta thickness versus radial distance slightly less steep along the centerpoint of a ray compared to what it is in the continuous ejecta blanket.

### 3.3. A Vertical Mixing Model for Craters Under the Resolution Limit of CTEM

The excavation flow model developed in section 3.1 accounts for the mixing and transport of material from craters that CTEM can resolve. Craters smaller than the size of a grid cell cannot be generated, and as a result, we lose information about how small craters affect material mixing. The mixing of material by small craters was investigated by *Gault et al.* [1974], who developed a framework for understanding the reworking zone based on Poisson statistics. They parameterized the time scale for the overturn of material by impacts as the time needed to cover a surface completely by craters of a given size. After a surface is completely covered by craters of size  $D_{\text{crat}}$  the whole area of the surface will have been mixed to a depth at which the deepest streamline in the excavation flow can reach, which *Gault et al.* [1974] took as  $D_{\text{crat}}/8$ . Because each cratering event occurs independently, regardless of crater size, the total overturning time scale is simply a superposition of overturning time scales of all craters in the crater production population.

To derive the probability that a surface has been excavated to some depth  $h$ , we developed a model similar to that of *Gault et al.* [1974] and also *Hirabayashi and Minton* [2017]. From Poisson statistics, *Gault et al.* [1974] found that for a model of a production population with a single crater size, the probability that any point on a cratered surface has been filled by craters that occupy an area of  $A = \pi r^2$  is

$$P(t) = 1 - \exp \left[ - \frac{dN(r)}{dr} A t \right], \quad (10)$$

where  $P(t)$  is the fraction of a surface occupied by craters with a radius  $r$  as a function of time  $t$  and  $\frac{dN(r)}{dr}$  is the number of craters that fall within the range of  $r$  and  $r + dr$  that form per unit area per unit time (the differential form of impact flux size-frequency distribution). Because each crater size has its own independent probability given by equation (10), the probability that the surface is covered by craters over the size range ( $r_{\text{min}} < r < r_{\text{max}}$ ):

$$P(r, t) = 1 - \exp \left[ - t \int_{r_{\text{min}}}^{r_{\text{max}}} \frac{dN(r)}{dr} A dr \right]. \quad (11)$$

For equation (11) we seek a fraction of a surface that is excavated to a depth. We assume that the shape of the excavation zone is approximately parabolic [*Melosh*, 1989]. Therefore, the excavation depth for each crater is given by a function,  $h(x, r)$ , which

$$h(x, r) = h_{\text{excav}} \left( 1 - \frac{x^2}{r^2} \right), \quad (12)$$

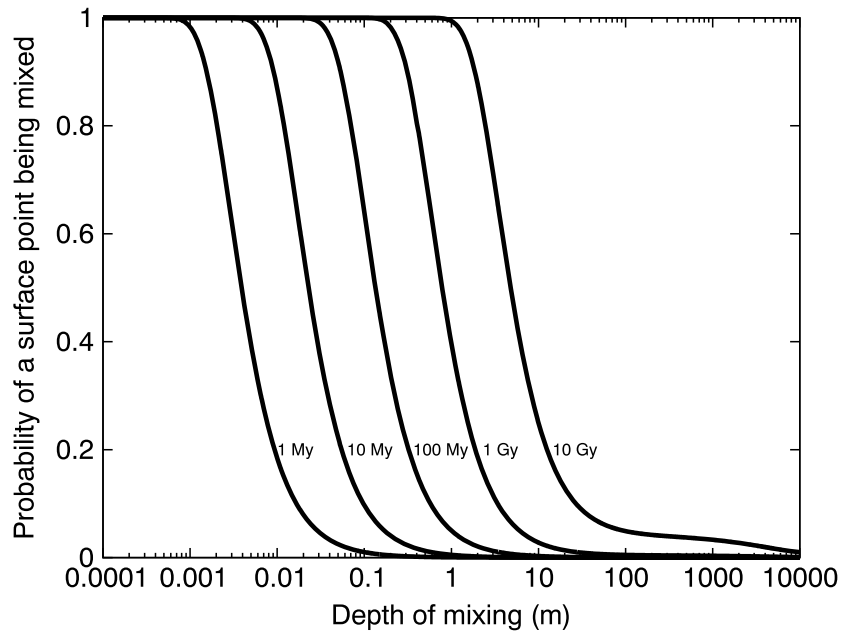


**Figure 6.** The fraction of surface that mixes to a given depth for a time interval from our vertical mixing model for subpixel-sized craters. The x axis is the mixing depth, and the y axis is the fraction of area that is mixed to that depth. Each curve is labeled with its corresponding time, 1 Myr, 10 Myr, 100 Myr, 1 Gyr, and 10 Gyr. For 1 Myr time interval, the probability of a surface that mixes to 1 cm (0.01 m) is <0.2, yet in that time, the whole surface has already mixed to 1 mm. Note that the 10 Gyr period at this constant impact flux rate is equivalent to a 3.65 Ga age accounting for the exponentially higher impact rate prior to ~3 Ga [Neukum et al., 2001].

where  $x$  is radial distance from the center of each crater of radius  $r$  and  $h_{\text{excav}}$  is the excavation depth at the crater center, which is where the excavation depth is a maximum. In this model, the area of the mixing zone in equation (11) is  $A = \pi x^2$ . Equation (11) becomes

$$P(r, t) = 1 - \exp \left[ -t \int_{r_{\min}}^{r_{\max}} \frac{dN(r)}{dr} \pi x^2 dr \right]. \tag{13}$$

We can link the relationship between a mixing zone and the size of a crater from equation (12),

$$\frac{x^2}{r^2} = \begin{cases} 1 - \frac{h}{h_{\text{excav}}}, & x < r \\ 0, & x \geq r. \end{cases} \tag{14}$$

The maximum excavation depth,  $h_{\text{excav}}$ , is given by  $h_{\text{excav}} = \alpha D = 2\alpha r$ , where  $\alpha$  is a parameter that sets the maximum excavation of a crater relative to its diameter. The value of  $\alpha$  can range from  $\alpha = 1/8$ , assuming that mixing is due to the excavation and deposition of the proximal ejecta blanket [Gault et al., 1974], to  $\alpha = 1/3$ , assuming that the area between the floor of the final crater and the floor of the transient crater is fully mixed [Collins, 2014]. In this study, we only consider the value of maximum excavation depth as  $h_{\text{excav}} = D_{\text{crat}}/8$  because our preliminary investigation for excavation depth as great as  $D_{\text{crat}}/3$  yields significant inconsistencies with the Clementine observational data. This may be because the region between the floor of the final crater and the floor of the transient crater is only partially mixed.

Equation (14) defines the mixing zone for a given crater size  $r$ , in which the mixing zone is limited to the radius of a crater. We then substituted equation (14) to  $A$  into equation (13), and we now have for our mixing probability equation:

$$P(h, t) = 1 - \exp \left[ -t \int_{\max(r_{\min}, \frac{h}{2\alpha})}^{r_{\max}} \frac{dN(r)}{dr} \pi r^2 \left( 1 - \frac{h}{2\alpha r} \right) dr \right]. \tag{15}$$

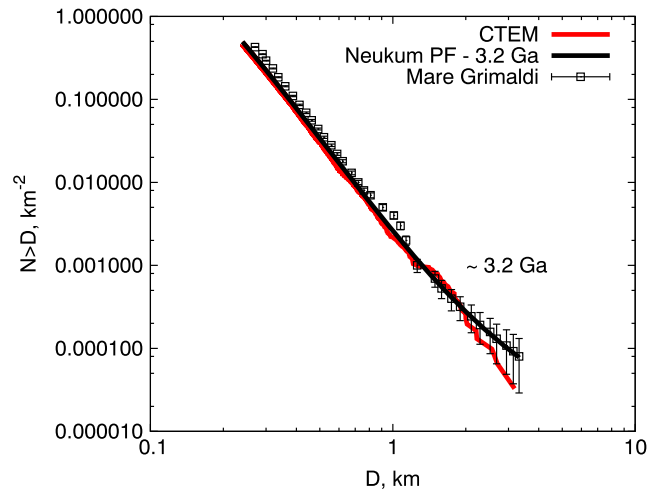


**Figure 7.** Crater size frequency distributions for the western Mare Grimaldi region. The solid black line shows the Neukum Production Function (NPF) age of 3.2 Gyr, and the red line shows the crater counts produced in our simulation with CTEM. The open square points with one sigma Poisson error bar ( $\sqrt{N}$ ) are based on crater counts from Greeley *et al.* [1993].

in 3.65 Ga is  $\sim 4$  m, which falls into the range of 2–10 m for typical regolith depth in mare regions [Oberbeck and Quaide, 1967, 1968; Quaide and Oberbeck, 1968, 1975; Oberbeck *et al.*, 1973; Bart *et al.*, 2011].

We use equation (15) to implement a subpixel vertical mixing model into CTEM. Our subpixel crater mixing model runs between each creation of a resolvable crater. For the time interval between a resolvable crater’s production, one can draw a probability function as shown in Figure 6. The short time interval gives a greater probability of a shallow mixing depth; however, there is a chance that a deeper mixing depth could occur. A random depth is drawn from the probability function given by equation (15) and then we create a mixed layer of material at each grid cell with this random depth.

#### 4. Mare/Highland Boundary Diffusion Simulation

Our goal is to model material transport by impacts at a mare/highland contact. We use the Clementine UV/VIS reflectance data set compiled by Li and Mustard [2000] for Grimaldi Crater as a constraint on our model, which shows a symmetric material fraction distribution on either side of the contact. We will also use the measured abundances of nonmare material within Apollo mare soil samples as additional constraints. These data are plotted in Figure 1. Then we will test the hypothesis of Li and Mustard [2000] that the 4–5 km width of the mixing zone across this contact is determined primarily by the transport of distal ejecta.

Grimaldi Crater is a 173 km diameter mare-filled crater and one of the four basins studied by Li and Mustard [2000]. Grimaldi Crater is located on the western shore of Oceanus Procellarum; thus, the lava that filled it is thought to have the same source as Oceanus Procellarum, which is the largest mare area on the Moon. The crater itself is a double-ring impact structure that is pre-Nectarian in age [Wilhelms, 1987]. Later Orientale basin-forming material, the Hevelius Formation, may have covered much of the Grimaldi region [Hawke *et al.*, 1995]. When the mare basaltic lava was initially emplaced, it formed a sharp boundary with the older anorthositic highland bedrock. The mare abundance at the center of the geological contact between Grimaldi’s mare and the surrounding highlands is about 50% [Li and Mustard, 2000], which suggests that the influence of large craters outside Grimaldi is not significant to the makeup of the regolith near the mare/highland contact.

Inside Grimaldi Crater, there is an up to 3.6 km thick mare basalt layer at the center of the crater, sitting atop of possible Orientale basin-forming ejecta and pre-Nectarian highland crustal material [Solomon and Head, 1980]. The largest crater found in the Mare Grimaldi is about 4 km in diameter (Figure 7), suggesting that locations where the mare basalt thickness is thinner than  $\sim 400$  m could have exposed the underlying highland material. However, we neglect this contamination of highland material because there are few large

The reason the lower limit on the integral in equation (15) can take two possible values is because at any given depth  $h$ , only craters with  $h_{\text{excav}} > h$  can contribute to mixing.

Using an input of time and a crater size frequency distribution, equation (15) allows us to calculate the probability that the regolith at depth  $h$  has been mixed at time  $t$ . Because equation (15) considers a constant impact flux, we can convert the time scale into actual time scale by using the Neukum chronology function [Neukum *et al.*, 2001]. Figure 6 shows the mixing depth probability at different time intervals (1 Myr–10 Gyr) under a constant impact flux rate. The 10 Gyr constant impact flux rate is equivalent to a 3.65 Ga age in the Neukum chronology [Neukum *et al.*, 2001]. Our median mixing depth

craters, and the contamination of highland material from the mare side to the highland side by these large craters would be insignificant. In addition, because the observed material fraction distribution is symmetrical across the contact, this local mixing of highlands from beneath the mare must be negligible; otherwise, the highland material fraction would be skewed toward the mare side.

#### 4.1. Mare/Highlands Contact Simulation Setup

For our simulation domain, we took the area of Grimaldi Crater ( $D=175$  km) as the total area of our simulated mare. We also assume that the size of our simulated highland is equal to the size of our simulated mare. Therefore, there are equal opportunities for cratering on both sides of the contact. Our simulated square grid dimensions are thus 175 km by 175 km, and our pixel resolution is equal to that of Clementine data at 120 m/pixel [see *Li and Mustard*, 2000, Table 2]. This gives us a 1460 pixel by 1460 pixel simulation domain, with a repeating boundary condition. The smallest crater we directly model is 1 pixel in diameter. For craters smaller than 120 m, we must use our subpixel crater mixing model, as described in section 3.3.

Our initially defined surface has a mare side on the left and a highland side on the right (see Figure 2). The mare side has one mare basalt layer that is 4 km thick, to match the observed thickness of the Grimaldi Crater mare [*Solomon and Head*, 1980], sitting on the top of the highland layer that has effectively infinite thickness. The highland side is one single layer that has infinite thickness of only highland material. We model the thickness of the mare layer as uniform and neglect the underlying shape of Grimaldi basin near the rim (gradual decrease of mare thickness toward the contact). If this thinning out of the mare near the boundary were important, we might expect an asymmetric material fraction distribution, with proportionally more highland material on the mare side. However, this is not observed in the data, and therefore, we assume that this component is future lunar missions. We also ignore topography differences between the mare and highland. Although the steeper slopes of the highlands along the contact would tend to transport material downward to the mare side, the material was only found to extend to several hundred meters for high slopes [*Young*, 1976], and again, one would expect the material distribution to be asymmetric at the boundary if this effect were important. This suggests that the slope effect of the highlands plays a less important role in transporting to the mare side, as the observed mixing zone has a scale of a few kilometers.

Our simulation time is set by the crater-derived age of the southwestern part of the mare deposit examined by *Li and Mustard* [2000], which is 3.2 Gyr old based on crater counts [*Greeley et al.*, 1993]. This region has no evidence for discrete resurfacing events occurring after the mare basalt emplacement. As mentioned in section 3, we use an impactor population and velocity distribution that result in a crater production function that is identical to the Neukum Production Function [*Neukum et al.*, 2001]. Figure 7 shows the crater size-frequency distribution from CTEM compared with both the crater counting study of *Greeley et al.* [1993] and the Neukum production function for a 3.2 Gyr old lunar surface. Note that the largest crater that we allow in a simulation is constrained by the Grimaldi Crater count so as to attempt to mimic Grimaldi Crater's western mare/highland contact. Because the compositional profile that *Li and Mustard* [2000] obtained from the western mare/highland contact of Grimaldi Crater does not include a crater larger than 4 km near the contact, we restricted our simulation to craters between 120 m (the grid cell resolution) and 4 km in diameter. Our subpixel mixing model considers the contribution from craters as small as 1 mm in diameter.

Our model includes multiple material transport mechanisms, as described in detail in section 3. These mechanisms include transport by distal ejecta (crater rays), transport by proximal ejecta of resolvable craters (continuous ejecta blankets), and mixing by subpixel craters (craters smaller than a grid cell). We performed four sets of simulations to test the hypothesis of *Li and Mustard* [2000] that distal ejecta control the width of the mixing zone across contacts like Grimaldi basin. These simulations are distinguished from each other by which components of our transport model are active. These simulations are proximal ejecta only with no subpixel crater mixing (Case A), proximal ejecta only with subpixel crater mixing (Case B), proximal and distal ejecta with no subpixel crater mixing (Case C), and proximal and distal ejecta with subpixel crater mixing (Case D). These different cases allow us to see the relative importance of each component of our model.

The simulation set, Case D, combines all components of our transport model and is closest to what the lunar surface experiences, while Case A is the most restricted and simulates only regolith transport due to

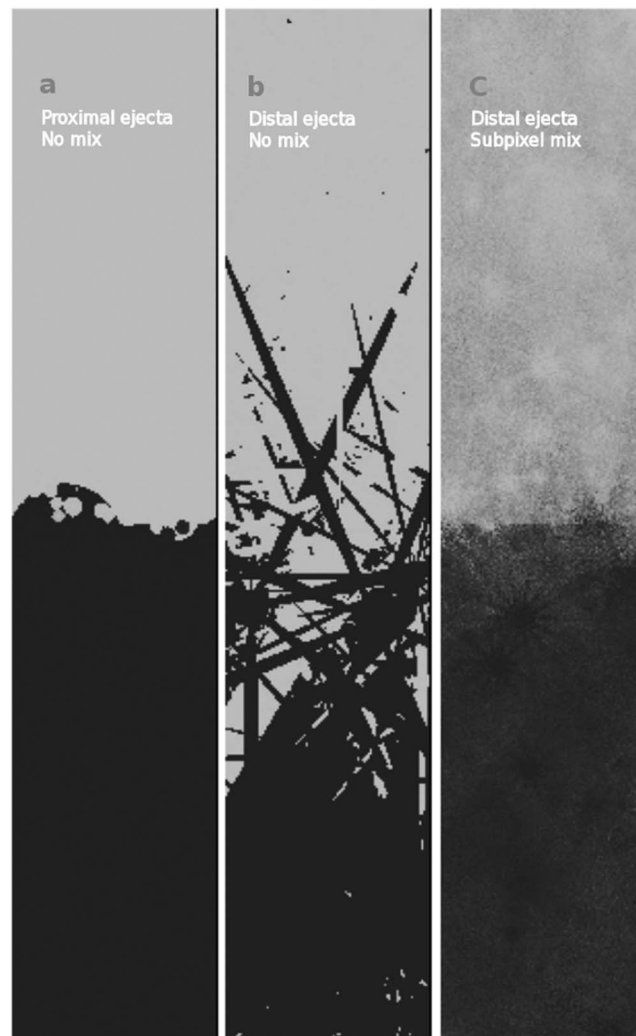


**Figure 8.** The mare fraction for Cases A, C, and D result (similar to Figure 5 in *Li and Mustard* [2000]). Each image is 200 by 1000 pixels. The lower part of the image represents the mare side, and the brighter part is the highland side. Each fraction image represents our simulation cases of (a) Case A (proximal ejecta with no subpixel crater mixing), (b) Case C (proximal and distal ejecta with no subpixel crater mixing), and (c) Case D (proximal and distal ejecta with subpixel crater mixing). Note that these mare fraction maps will not visually match the appearance of contacts on the lunar surface because it does not take into account optical maturation of rays with time.

material is barely transported across the boundary (Case A). Only a crater that is close to the edge of the mare/highland contact would deposit its continuous ejecta across the contact. Assuming that a 1 km diameter crater occurs at the contact, it would create ~2 km of continuous ejecta across the contact. The probability of a few km diameter crater occurring at the contact is relatively small, and it appears that such a crater has not occurred to our study area (mare/highland contact of southwestern Grimaldi Crater) at least from the observation of Clementine data. In fact, the contribution of a few km diameter crater at the contact to the exotic component would be smoothed out by averaging methods that are used in processing Clementine data and our simulation results. As a result, the material transport of proximal ejecta in Cases A and B appears limited.

Figure 8b shows a mixing zone that is ~10 km wide for Case C. The sharp boundary seen in Cases A and B is now crossed by rays. The contrast is high between rays and background surface material (mare or highland

resolvable craters. The Case D simulation is also closest to what *Li and Mustard* [2000] assumed for their anomalous diffusion model and includes all components. Their distal ejecta-dominated anomalous diffusion model allows them to consider craters down to microns in size, which is the scale of our subpixel crater mixing model. More importantly, with a better treatment of the spatial distribution of distal ejecta, our results enable us to investigate discrepancy between the two different observations: the narrow (4–5 km) and wide (>20 km) mixing zones seen in the data (Figure 1). All simulation results will be compared with Clementine UV/VIS camera reflectance data and Apollo mare soil samples.

#### 4.2. Results of Our Mare/Highland Contact Simulations

The initial mare and highland contact is sharp, with the pure mare on the left-hand side and the pure highland on the right-hand side. For each case described in section 4.1, we performed one run with the same random seed in CTEM. In all of our simulation cases the mare/highland boundary becomes more diffuse with time, but the amount of transported material across the contact depends on which components of our transport model are active.

In Figure 8, fraction images from each case show how the contact is changed by adding a component in the model. For example, the mixing zone in the proximal ejecta-only models (Cases A and B) is always limited to <1 km wide. Figure 8a shows that the mare/highland contact remains sharp, and exotic

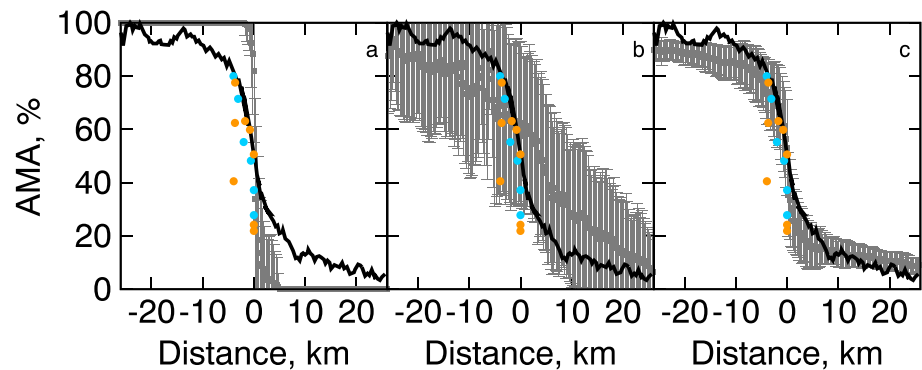


**Figure 9.** The compositional gradient profile of the average mare abundance (AMA) within a distance of 26 km from mare (left-hand side) and highland (right-hand side) contact. The black line represents the Clementine data for Grimaldi Crater from *Li and Mustard* [2000]. The solid square point in gray color in each box represents the mean AMA of the total 1441 profiles from each case of (a) Case A, (b) Case C, and (c) Case D. One standard deviation across the contact is shown by a vertical line at every solid square point. The solid points in orange and blue color are Apollo 15 and 17 in situ mare soil samples from Figure 1 in *Rhodes* [1977], respectively.

side). The fresh appearance of rays at the contact would be similar to how a ray may appear as soon as it forms and before small crater gardening mixes and dilutes the exotic material. Because small crater gardening is not modeled in Case C, any exotic material in a ray stays at the surface until a subsequent excavation or deposition occurs. Figure 8c shows the fuzzy appearance of the boundary in our Case D simulation, in which subpixel mixing is turned on. When we turn on subpixel mixing in Case D, the transported exotic material gets reworked into the local regolith and the surface albedo looks much closer to the natural surface at the Grimaldi crater contact.

To quantitatively compare our simulation results with Clementine data, we obtained a compositional gradient profile similar to that which *Li and Mustard* [2000] used to analyze all four basin measurements taken by the Clementine UV/VIS camera. The compositional gradient profile describes the mare abundance at a specific distance from the mare/highland contacts, and one can plot how the mare abundance changes with distance from the contacts. For each compositional gradient profile, *Li and Mustard* [2000] extracted reflectance values averaged over 20 pixels, each at a specific distance from a mare/highland contact, to mitigate the effects of noise of Clementine UV/VIS reflectance measurements, variability in apparent reflectance due to surface roughness, and other pixel-scale sources of stochastic variability. They created only two compositional gradient profiles for each of the four basins. In each of our simulations, we ran through all pixels parallel to the contact and collected 1441 profiles in which each profile is averaged over 20 pixels to enable direct comparison with *Li and Mustard's* measurements. We can calculate the mean mare abundance at a specific distance from those 1441 profiles as well as the standard deviation of mare abundance. Figure 9 shows the average mare abundance and one standard deviation among all 1441 profiles for each case.

The results of the Cases A and B simulations, which include only continuous ejecta, lead to a mixing zone less than 1 km in width, closely consistent with the classical diffusion model of *Li et al.* [1997] (Figure 9a). In Figures 9b and 9c, the Cases C and D simulations, which include both continuous and distal ejecta, have mixing zones wider than 1 km. The Case C result (Figure 9b) contains the largest width of mixing zone, up to 10 km on a side. This is much wider than the Clementine UV/VIS measurement for Grimaldi Crater's contact. Case C also has the largest variation of mare abundance across the contact, indicating that the compositional gradient profile is highly affected by distal ejecta in rays. As a result, the dependence of mare abundance on the sampling distance is the smallest.

As we added the subpixel crater mixing component and, eventually, the ray mixing component into Case C, the result of Case C shows a larger variability of composition across the contact than in Case D. With consideration of subpixel craters mixing, the mean mare abundances across the contact show a match with Clementine data. The addition of subpixel crater mixing component in Case D is important because both rework the resolvable crater ejecta deposits that are only generated in Case C. Among resolvable crater ejecta deposits, their crater rays often transport exotic material across mare/highland contacts; thus, their deposits are relatively less mixed.

Because the scale of excavation depth for a resolvable crater that generates crater rays is usually larger than the thickness of preexisting ejecta layers created by previous impacts, it deposits mostly pure exotic material to the other side. When subpixel crater mixing and ballistic sedimentation are neglected (Case C), both proximal and distal ejecta stay on the surface. For the same deposit, but with the subpixel craters mixing model enabled (Cases D), the subsequent small impacts or energetic ejecta penetrate through this ejecta deposit layer and mix it with the underlying local (nonexotic) material. In this case, the exotic component becomes mixed with local material, leading to a lower exotic abundance compared to the exotic abundance in Case C. Thus, as expected, Case C results in a higher exotic component at the surface on either side of the contact (Figure 9b). The role of both the subpixel crater mixing model is to process (and dilute) distal material. A significant reduction of the exotic component on both sides of the contact in Case D result can be explained by this diluting process. Both results suggest that all scales of craters are important to determine what material is at the surface across the Moon, as well as the ultimate fate of material transported across contacts.

The variability of mare abundance in results from Case D is smaller than in Case C because subpixel crater mixing may bury fresh distal material. For example, the range of one standard deviation in the Case C simulation result completely encompasses the variability of mare abundance revealed in both Apollo 15 and 17 mare soil samples (see Figure 9b). Yet the average mare abundance from Case C is highly inconsistent with the observed compositional profile of Clementine data. On the other hand, the Apollo 15/17 sample data are within the error bars of the Case D results, except for one data point at the distance of 4 km, only 40%, compared to the average mare abundance of 60–80% of the other soil samples. The Case D simulation results show a slightly higher exotic abundance on both sides than the Clementine data.

In general, the majority of spatial variation of composition within this 4–5 km wide mixing zone can be accounted for by local craters near the mare and highland contact. Beyond the local scale, the stochastic nature of cratering process sometimes means that large specific craters act as a source for exogenic material that is transported more broadly and may be present in many mare soil samples. For example, there are two Apollo 15 mare soil samples (15101 and 15923) collected at stations 2 and 6 closer to the contact (Apennine Front) with low mare abundances (<30%). Their relatively high nonmare abundances could be associated with a ray from nearby craters Aristillus or Autolycus, which were large enough to excavate below the mare [Carr *et al.*, 1971; Lunar Sample Preliminary Examination Team (LSPET), 1972; Spudis and Ryder, 1985]. Russ *et al.* [1972] used low-energy fluence data from the Apollo 15 drill core (the lunar module site) to show that there was no indication of the ray deposition, which contradicts the explanation of ray material in a sample. The distances from Autolycus or Aristillus Crater to the Apollo 15 landing site are 150 km and 250 km respectively, which are greater than the length of our simulation domain. Craters of similar diameter, ~39 km for Autolycus Crater and ~55 km for Aristarchus Crater, were not generated in our simulation. Large craters may have randomly thrown a broad ray patch containing considerable amounts of nonmare material or KREEP material to the landing site (see section 6). As a result, the higher nonmare abundance observed in the mare soil sample collected at the Apollo 15 lunar module site might have been affected by a ray from a large crater beyond the local scale of the mare and highland contact.

## 5. Implications of Our Impact Transport Model for Evolution of Lunar Surface Materials

Based on comparisons of our Case C and Case D results, we suggest that larger craters are capable of delivering exotic material to a distal location, while small and local craters serve to bury those exotic and distal ejecta materials (due to reworking and mixing). Without large craters, exotic material from one side of the mare/highland contact cannot reach the other side. Once those distal ejecta materials arrive at the other side, they are buried or comminuted or recycled by local small craters. The combination of these two transport processes leads to this 4–5 km wide mixing zone. Our new three-dimensional regolith transport model provides more detail about how impacts transport material over the lunar surface.

For all of our simulation results, mean mare abundance profiles at an equivalent distance of the Apollo 11 and 12 landing sites (Luna 16 is beyond our simulated mare domain) remain >90%; therefore, the nonmare abundance is less than 10%. All our final results (Figure 9) appear to fail to explain the elevated nonmare abundances present in Apollo 11 and 12 and Luna 16 mare soil samples. The <10% of nonmare

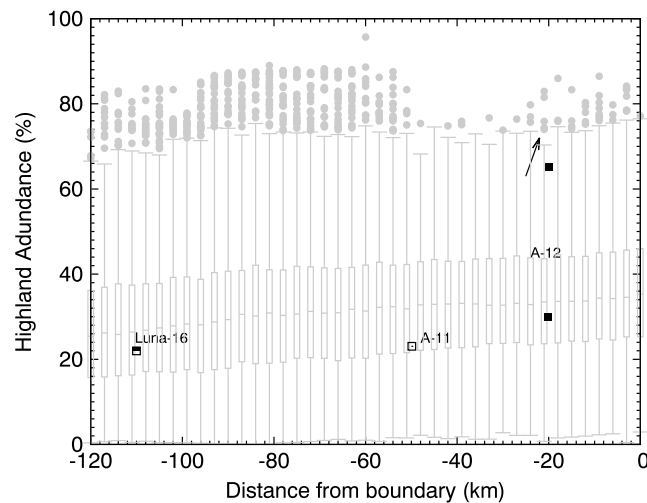


**Figure 10.** The exotic component (highland) distribution with distance from mare and highland contact from our global run result. Composition distribution at a distance is plotted as a box and whisker plot. The line inside of the box is the median value of total composition distribution at a given distance. The upper and lower boundaries of the box represent the 25% of data above the median and the 25% of data below the median, respectively. The ends of the whiskers represent 99% of data. The solid circles in light gray color are outliers. The data points in black color with labels of “A-12,” “A-11,” and “Luna-16” are from Apollo 12 and 11 and Luna 16 mare, respectively, soil samples. The black arrow denotes one example of a ray patch in our simulation domain (see close-up in Figure 12).

out spatially dependent anomalies of nonmare abundance that result from crater rays caused by the random nature of the cratering process.

*Li and Mustard* [2005] suggested that large craters  $>100$  km away from contacts may explain the elevated nonmare abundance of  $>20\%$  in most mare soil samples. To test this large crater hypothesis, we performed a global run to account for the effect of larger craters at large distances from the mare/highland contact. Ideally, it would be best to test how large craters distribute their distal ejecta on a spherical globe, yet at present, CTEM cannot account for lunar curvature. In this study, we simulated the global lunar surface as 6000 km by 6000 km square, which is 2000 pixels by 2000 pixels at a resolution of 3 km/pixel. Our global square is 17% mare plains and 83% highlands [Head and Wilson, 1992]. We assume that the contamination of the underlying highland material beneath our global mare layer to a mare soil sample can be neglected. This assumption allows us to see the contribution of distal ejecta from larger craters to mare soil samples without worrying about locally excavated contamination.

We set the thickness of mare in our global domain as 4 km and the underlying highland material that is effectively infinitely deep. On the highland side, there is a single layer of highland material. In our global run, we produced about eight large craters (100–200 km) in total, and the larger craters ( $>160$  km) occur at our global highland side. Figure 12 shows broad and long rays from  $D > 160$  km craters crossing the global mare/highland contact. On the other hand, there were a few craters on the order of  $\sim 100$  km that formed on the mare side of our global run (close to mare/highland contact at the bottom). For example, a crater from the mare side that is close to the mare/highland contact at the bottom in Figure 12 excavates to the underlying highland material, leaving a bright crater floor on the mare side.

Figure 10 shows the highland component transported to the mare in our global run. We use the box and whisker plot to present the distribution of highland component at a given distance. With a resolution of 3 km in our global domain, each box represents the total distribution of 2000 pixels at a given distance from the contact. The upper and lower boundaries of the box represent the 25% of total pixels above the median and the 25% of total pixels below the median, respectively. The error bars bound 99% of total pixels. Outliers are shown

abundance in our simulation is about half that of Apollo 11 and 12 and Luna 16 mare soils ( $>20$ – $70\%$ ), even though we take into account the variation of nonmare abundance in Case C (the largest variation of all cases).

Our results suggest that the primary difference between the Clementine data for the contact of Grimaldi Crater and Apollo 11 and 12 and Luna 16 mare soil samples is sampling scale. The remote sensing data, and our simulation results, are averaged over a spatially extended region of  $\sim 120$  m, while the scale of Apollo 11 and 12 and Luna 16 mare soil samples is limited to a handful amount of soils (centimeter, finer scale compared to the order of 100 m) at “astronaut” scales ( $\sim$ m). This scale discrepancy between data sets at these different spatial scales may be a direct result of the high spatial heterogeneity inherent in distal transport of ejecta because it is concentrated into rays. The averaging methods that were used in our simulations and the processed Clementine data might have smoothed

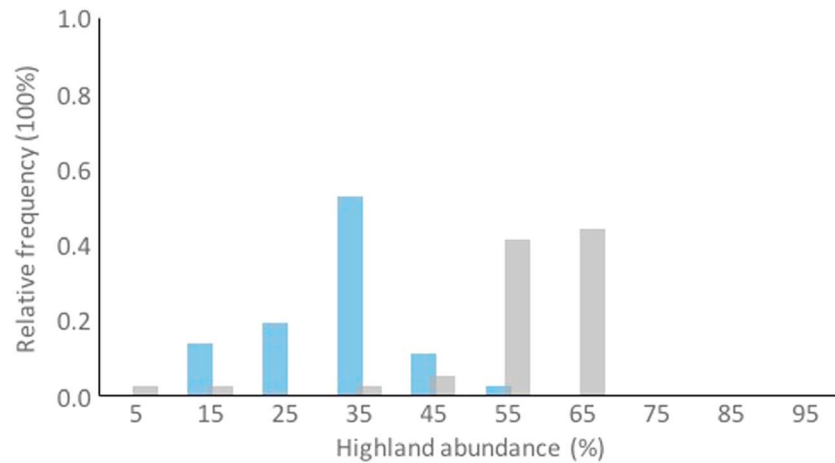


**Figure 11.** Histogram of highland abundance normalized by the total number of pixels inside a ray patch and nonray region shown in Figure 12. The bars in blue color are the nonray region population (36 pixels in total) in our global run, while the bars in gray color are the population sampled from a localized ray patch in our simulation result (36 pixels in total).

outside the error bars. As shown in Figure 10, the typical highland abundances from the Apollo 11 and 12 and Luna 16 mare soil samples fall within the majority of the population at a given sampling distance. In detail, the median nonmare abundances from our simulation result are slightly higher than the nonmare abundance of the Apollo 11 and 12 and Luna 16 mare soil samples. For example, Figure 10 shows ~30% of median nonmare abundance at our simulated Apollo 12 landing site and ~26% for our simulated Luna 16 landing site.

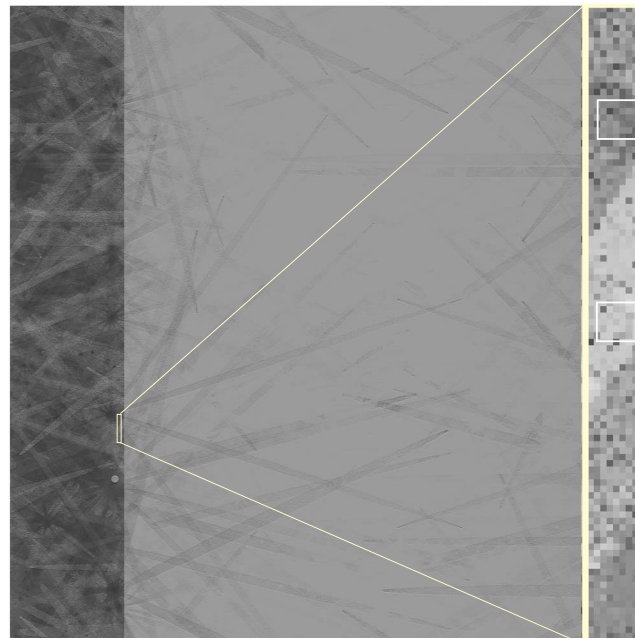


**Figure 12.** Compositional map of our global mare/highland contact run with all model components turned on. The simulation size is 6000 km by 6000 km (2000 by 2000 pixels). The yellow arrow points to a ray patch at an equivalent distance of the Apollo 12 sites from our simulated mare/highland contact. The inset on the left-hand side is the close-up of the ray patch and nonray region on the right-hand side. Inside close-up, the square white box on the top is nonray region, and the square white box on the bottom is almost the center of ray patch.

Figure 11 shows the relative frequency of nonmare abundance for both the nonray region and the extremely localized ray in proximity to the Apollo 12 landing site. We show an example of 8 pixel wide ray at this distance (see the yellow rectangular on the left-hand side of Figure 12). We highlighted ray and nonray regions to see both distributions of highland material abundance (see the white square boxes on the right-hand side of Figure 12). The highland abundances in ray and nonray regions exhibit a bimodal distribution (Figure 11). In nonray region (top white box in the inset of Figure 12), about 70% of all pixels (36 pixels) span 20–40% highland abundance and 14% of pixels have 10–20% highland abundance. In contrast, the ray region (bottom white box in the inset of Figure 12), consisting of 36 pixels, has >80% of pixels with the range of 50 and 70% of highland abundance. This simulated Apollo 12 landing site is similar to the Apollo 12 landing site because the Apollo 12 landing site is seen superposed by a Copernicus ray [LSPET, 1970].

Thus, the easiest explanation is that the exceptionally high nonmare abundance at Apollo 12 is a result of spatial heterogeneity caused by a ray from Copernicus Crater. *Hubbard et al.* [1971] also proposed that the KREEP material seen in these samples arrived by means of distal ejecta/rays from Copernicus Crater and the Fra Mauro region [Meyer and Hubbard, 1970; Meyer et al., 1971]. For example, the Apollo 12 12033 soil sample was sampled from the bottom of a 15.24 cm deep trench near the north rim of Head Crater, and 66% of the glass fragment from the 12033 sample is KREEP material. The Apollo 12 12070 soil taken from the north side of Surveyor Crater is 25% KREEP [Hubbard et al., 1971]. It is clear that the nonmare component within a ray patch contains a portion of pure highland material mixed with local mare basalt. More importantly, our modeling demonstrates that the abundance of exotic material at specific locations is highly variable spatially.

These arguments strengthen the case that the highly elevated abundances in nonmare material in certain Apollo 12 samples are attributable to Copernicus Crater and that the attribution of the ~800 Ma age of Apollo 12 KREEPy samples to Copernicus is correct [Bogard et al., 1994; Barra et al., 2006]. This is significant because of Copernicus's role as a potential anchor point for lunar chronology [Stoffler et al., 2006; Hiesinger et al., 2012].

## 6. Conclusion

Both proximal and distal ejecta transported by impacts are important to the distribution of material across the lunar surface. To separate the effect of local and distal ejecta on the material exchanged across contacts, we modeled three main components: proximal/distal ejecta, subpixel crater mixing, and ray/ejecta mixing. By adding each component one-by-one to our model, we investigated how craters formed in proximity to the mare/highland contact influence the compositional variation within the 4–5 km wide mixing zone. Our regional run results (Case D) can explain observed changes in composition across mare and highland contacts that are seen in Clementine data. As the average mare abundances of the Case D results are consistent with the Clementine data, the varying mare abundances seen in the Case D simulation can also explain the majority of mare abundances of Apollo 15/17 soil samples. Low nonmare abundances are present in our simulated Apollo 11 and 12 landing sites unless we take into account the contribution of specific large craters (e.g., Copernicus Crater) that appear to contribute to the global elevated nonmare abundance.

As seen in the patchy rays in our global model result (Figure 12), the superposition of large crater rays may result in the elevated nonmare abundance in mare soil samples. Crater ray deposits, particularly from large craters, are a source of exotic material, and this exotic material is then either distributed or diluted by smaller craters as time passes. As these processes proceed, mare soils become more contaminated by anorthositic material, and a sample scooped from a mare plain is likely to include this reworked material. However, when the Apollo missions landed at places superposed by rays and close to specific large young craters, the chance of acquiring samples of this ray material was greatly enhanced (much more so than the chance of collecting "average" mare). The fact that this material was patchy and localized and only a few Apollo 12 soil samples had much higher concentration of nonmare materials is consistent with our understanding of the transport and mixing process. Thus, our results support the earlier interpretation that Copernicus Crater ray was the source of highland material at the Apollo 12 landing site area, contaminating and skewing the mare soil and regolith record. The Copernicus Crater ray material in Apollo 12 mare soil samples is an example of the stochastic nature of the cratering process and demonstrates how a large crater can affect even distant landing sites' samples. It would be useful for future lunar missions to test whether or not the elevated nonmare abundance seen in Apollo 11 and 12 and Luna 16 samples and orbital data is biased by rays by sampling at regions with less contamination by rays.

An example of a region with less complicated geology is the contact between mare and highlands in the western part of Grimaldi Crater. Our model is able to reproduce the 4–5 km width of the mixing zone in this region and demonstrates that both distal and proximal ejecta materials are important for regolith evolution.

## References

- Arvidson, R., R. J. Drozd, C. M. Hohenberg, C. J. Morgan, and G. Poupeau (1975), Horizontal transport of the regolith, modification of features, and erosion rates on the lunar surface, *Moon*, 13(1–3), 67–79, doi:10.1007/BF00567508.
- Baldwin, R. B. (1963), *The Measure of the Moon*, 1st ed., 488 pp., Univ. of Chicago, Chicago.
- Barra, F., T. D. Swindle, R. L. Korotev, B. L. Jolliff, R. A. Zeigler, and E. Olson (2006), 40Ar/39Ar dating of Apollo 12 regolith: Implications for the age of Copernicus and the source of nonmare materials, *Geochim. Cosmochim. Acta*, 70(24), 6016–6031, doi:10.1016/j.gca.2006.09.013.

### Acknowledgments

This work is supported by NASA Earth and Space Sciences Fellowship (NESSF) and the NASA Solar System Workings program (grant NNX15AL41G). Any additional data may be obtained from the corresponding author (huang474@purdue.edu). All lunar samples that we used are cited in main text, and an interested reader may refer to the reference list. We especially thank associate editor Gareth Collins, Carle M. Pieters, and the anonymous reviewer for all helpful suggestions and comments that improved the final manuscript.

- Bart, G. D., R. D. Nickerson, M. T. Lawder, and H. J. Melosh (2011), Global survey of lunar regolith depths from LROC images, *Icarus*, 215(2), 485–490, doi:10.1016/j.icarus.2011.07.017.
- Bogard, D. D., D. H. Garrison, C. Y. Shih, and L. E. Nyquist (1994), 39Ar-40Ar dating of two lunar granites: The age of Copernicus, *Geochim. Cosmochim. Acta*, 58(14), 3093–3100, doi:10.1016/0016-7037(94)90181-3.
- Borg, J., G. M. Comstock, Y. Langevin, and M. Maurette (1976), A Monte Carlo model for the exposure history of lunar dust grains in the ancient solar wind, *Earth Planet. Sci. Lett.*, 29(1), 161–174, doi:10.1016/0012-821X(76)90036-4.
- Budney, C. J., and P. G. Lucey (1998), Basalt thickness in Mare Humorum: The crater excavation method, *J. Geophys. Res.*, 103(E7), 16,855–16,870, doi:10.1029/98JE01602.
- Carr, M. H., K. A. Howard, and F. El-Baz (1971), Geologic maps of the Apennine-Hadley region of the Moon, map 1-72, U.S. Geol. Surv. Washington, D. C.
- Collins, G. S. (2014), Numerical simulations of impact crater formation with dilatancy, *J. Geophys. Res. Planets*, 119, 2600–2619, doi:10.1002/2014JE004708.
- De Hon, R. A. (1974), Thickness of mare material in the Tranquillitatis and Nectaris basins, *Proc. Fifth Lunar Conf.*, 1, 53–59.
- Duncan, A. R., M. K. Sher, Y. C. Abraham, A. J. Erlank, J. P. Willis, and L. H. Ahrens (1975), Compositional variability of the Apollo 15 regolith, *6th Lunar Sci. Conf.*, 6, 220–222.
- Elliott, J., Y.-H. Huang, D. A. Minton, and A. M. Freed (2016), The length of lunar crater rays explained using secondary crater scaling, in 47th Lunar and Planet. Sci. Conf.
- Evans, A. J., J. M. Soderblom, J. C. Andrew-Hanna, S. C. Solomon, and M. T. Zuber (2016), Identification of buried lunar impact craters from GRAIL data and implications for the nearside Maria, *Geophys. Res. Lett.*, 43, 2445–2455, doi:10.1002/2015GL067394.
- Farrand, W. H. (1988), Highland contamination and minimum basalt thickness in northern Mare Fecunditatis, *Proc. Lunar Planet. Sci. Conf. 18th*, 319–329.
- Fischer, E. M., and C. M. Pieters (1995), Lunar surface aluminum and iron concentration from Galileo solid state imaging data, and the mixing of mare and highland materials, *J. Geophys. Res.*, 100(E11), 23,279–23,290, doi:10.1029/95JE02359.
- Gault, D. E., and J. A. Wedekind (1978), Experimental studies of oblique impact, in *Proc. Lunar Sci. Conf. 9th*, vol. 9, pp. 3843–3875, Pergamon Press, New York.
- Gault, E. D., F. Horz, E. D. Brownlee, and B. J. Hartung (1974), Mixing of the lunar regolith, *Proc. Fifth Lunar Conf.*, 3, 2365–2386.
- Gielis, J. (2003), A generic geometric transformation that unifies a wide range of natural and abstract shapes, *Am. J. Bot.*, 90(3), 333–338, doi:10.3732/ajb.90.3.333.
- Goles, G. G., A. R. Duncan, D. J. Lindstrom, M. R. Martin, R. L. Beyer, M. Osawa, K. Randle, L. T. Meek, T. L. Steinborn, and S. M. McKay (1971), Analyses of Apollo 12 specimens: Compositional variations, differentiation processes, and lunar soil mixing models, *Proc. 2nd Lunar Sci. Conf.*, 2, 1063–1081.
- Greeley, R., et al. (1993), Galileo imaging observations of lunar Maria and related deposits, *J. Geophys. Res.*, 98(E9), 17,183–17,205, doi:10.1029/93JE01000.
- Hawke, B. R., C. A. Peterson, P. G. Lucey, and C. R. Coombs (1995), Remote sensing studies of the Grimaldi region of the Moon, *Lunar Planet. Sci. XXVI*, 26, 561–562.
- Hawke, B. R., D. T. Blewett, P. G. Lucey, C. A. Peterson, B. A. Campbell, and M. S. Robinson (1999), The compositional and origin of selected lunar crater rays, *Work. New Views Moon II*, 22.
- Head, J. W. (1982), Lava flooding of ancient planetary crusts—Geometry, thickness, and volumes of flooded lunar impact basins, *Moon Planets*, 26, 61–88, doi:10.1007/BF00941369.
- Head, J. W., and L. Wilson (1992), Lunar mare volcanism: Stratigraphy, eruption conditions, and the evolution of secondary crusts, *Geochim. Cosmochim. Acta*, 56(6), 2155–2175, doi:10.1016/0016-7037(92)90183-J.
- Hiesinger, H., C. H. Van Der Bogert, J. H. Pasckert, L. Funcke, L. Giacomini, L. R. Ostrach, and M. S. Robinson (2012), How old are young lunar craters?, *J. Geophys. Res.*, 117, E00H10, doi:10.1029/2011JE003935.
- Hirabayashi, M., and D. A. Minton (2017), An analytical model of crater count equilibrium, *Icarus*, doi:10.1016/j.icarus.2016.12.032.
- Holsapple, K. A. (1993), The scaling of impact processes in planetary sciences, *Annu. Rev. Earth Planet. Sci.*, 21, 333–373.
- Horz, F. (1978), How thick are lunar mare basalts?, *Proc. Lunar Sci. Conf. 9th*, 3311–3331.
- Housen, K. R., R. M. Schmidt, and K. A. Holsapple (1983), Crater ejecta scaling laws: Fundamental forms based on dimensional analysis, *J. Geophys. Res.*, 88(B3), 2485–2499, doi:10.1029/JB088iB03p02485.
- Howard, K., and H. G. Wilshire (1973), Flows of impact melt at lunar craters, *Abstr. Lunar Planet. Sci. Conf.*, 4, 389.
- Howard, K. A. (1974), Fresh lunar impact craters: Review of variations with size, *Proc. Fifth Lunar Conf.*, 1(5), 61–69.
- Hubbard, N. J., C. Meyer, P. W. Gast, and H. Wiesmann (1971), The composition and derivation of Apollo 12 soils, *Earth Planet. Sci. Lett.*, 10(3), 341–350, doi:10.1016/0012-821X(71)90040-9.
- Labotka, T. C., M. J. Kempa, C. White, J. J. Papike, and J. C. Laul (1980), The lunar regolith: Comparative petrology of the Apollo sites, *Proc. Lunar Planet. Sci. Conf. 11th*, 1285–1305.
- Laul, J. C., and J. J. Papike (1980), The lunar regolith: Comparative chemistry of the Apollo sites, in *Proc. Lunar Planet. Sci. Conf. 11th*, pp. 1307–1340, Pergamon Press, New York.
- Li, L., and J. F. Mustard (2000), Compositional gradients across mare-highland contacts: Importance and geological implication of lateral transport, *J. Geophys. Res.*, 105(E8), 20,431–20,450, doi:10.1029/1999JE001168.
- Li, L., and J. F. Mustard (2005), On lateral mixing efficiency of lunar regolith, *J. Geophys. Res.*, 110, E11002, doi:10.1029/2004JE002295.
- Li, L., J. M. Mustard, and G. He (1997), Compositional gradients across mare-highland contacts: The importance of lateral mixing, *Lunar Planet. Sci. XXVIII*.
- Lunar Sample Preliminary Examination Team (LSPET) (1970), Preliminary examination of lunar samples from Apollo 12, *Science*, 167(3923), 1325–1339, doi:10.1126/science.167.3923.1325.
- LSPET (1972), The Apollo 15 lunar samples: A preliminary description, *Science*, 175(4020), 363–375.
- Maxwell, D., and K. Seifert (1974), Modeling of cratering, close-in displacements, and ejecta, *Tech. rep.*, Def. Nucl. Agency, Washington, D. C.
- Maxwell, D. E. (1977), Simple Z model for cratering, ejection, and the overturned flap, *Impact Explos. Cratering Planet. Terr. Implic.*, 1, 1003–1008.
- McKay, D., G. Heiken, A. Basu, G. Blanford, S. Simon, R. Reedy, B. M. French, and J. Papike (1991), The lunar regolith, in *Lunar Sourcebook*, edited by G. Heiken et al., pp. 285–356, Cambridge Univ. Press, Cambridge, U. K.
- McKay, D. S., G. H. Heiken, and G. Waits (1978), Core 74001/2 grain size and petrology as a key to the rate of in-situ reworking, *Proc. Lunar Sci. Conf. 9th*, 1913–1932.

- Melosh, H. J. (1989), *Impact Cratering: A Geologic Process*, 245 pp., Oxford Univ. Press, New York.
- Meyer, C. J., and N. J. Hubbard (1970), High potassium, high phosphorous glass as important rock type in the Apollo 12 soil samples, *Meteoritics*, 5(9), 210–211.
- Meyer, C. J., R. J. Brett, N. J. Hubbard, D. A. Morrison, D. S. McKay, F. K. Aitken, H. Takeda, and E. Schonfeld (1971), Mineralogy, chemistry, and origin of the KREEP component in soil samples from the ocean of storms, *Proc. 2nd Lunar Sci. Conf.*, 1, 393–411.
- Minton, D. A., J. E. Richardson, and C. I. Fassett (2015), Re-examining the main asteroid belt as the primary source of ancient lunar craters, *Icarus*, 247, 172–190, doi:10.1016/j.icarus.2014.10.018.
- Moore, H. J., and R. B. Baldwin (1968), Ranger VIII and gravity scaling of lunar craters, *Science*, 159, 333–334.
- Morris, R. (1978), In situ reworking (gardening) of the lunar surface: Evidence from the Apollo cores, *Proc. Lunar Planet. Sci. Conf.* 9th, 1801–1811.
- NASA Technical Report Server (1972), Apollo 15 preliminary science report.
- NASA Technical Report Server (1973), Apollo 17 preliminary science report.
- Neukum, G., B. A. Ivanov, and W. K. Hartmann (2001), Cratering records in the inner solar system in relation to the lunar reference system, *Space Sci. Rev.*, 96, 55–86.
- Nozette, S., et al. (1994), The Clementine mission to the Moon: Scientific overview, *Science*, 266(5192), 1835–1839, doi:10.1126/science.266.5192.1835.
- Oberbeck, V. R. (1975), The role of ballistic erosion and sedimentation in lunar stratigraphy, *Rev. Geophys.*, 13(2), 337–362, doi:10.1029/RG013i002p00337.
- Oberbeck, V. R., and W. L. Quaide (1967), Estimated thickness of a fragmental surface layer of Oceanus Procellarum, *J. Geophys. Res.*, 72(18), 4697–4704, doi:10.1029/JZ072i018p04697.
- Oberbeck, V. R., and W. L. Quaide (1968), Genetic implications of lunar regolith thickness variations, *Icarus*, 9(1–3), 446–465, doi:10.1016/0019-1035(68)90039-0.
- Oberbeck, V. R., W. L. Quaide, M. Mahan, and J. Paulson (1973), Monte Carlo calculations of lunar regolith thickness distributions, *Icarus*, 19(1), 87–107, doi:10.1016/0019-1035(73)90141-3.
- Pieters, C. M., J. B. Adams, M. O. Smith, P. J. Mouginiis-Mark, and S. H. Zisk (1985), The nature of crater rays: The Copernicus example, *J. Geophys. Res.*, 90(B14), 12,393–12,413, doi:10.1029/JB090iB14p12393.
- Quaide, W., and V. Oberbeck (1975), Development of the mare regolith: Some model considerations, *Moon*, 13(1–3), 27–55, doi:10.1007/BF00567506.
- Quaide, W. L., and V. R. Oberbeck (1968), Thickness determinations of the lunar surface layer from lunar impact craters, *J. Geophys. Res.*, 73(16), 5247–5270, doi:10.1029/JB073i016p05247.
- Rhodes, J. M. (1977), Some compositional aspects of lunar regolith evolution, *Philos. Trans. R. Soc. A Math. Phys. Eng. Sci.*, 285(1327), 293–301, doi:10.1098/rsta.1977.0068.
- Rhodes, J. M., K. V. Rodgers, C. Shih, B. M. Bansal, and L. E. Nyquist (1974), The relationships between geology and soil chemistry at the Apollo 17 landing site, *Proc. 5th Lunar Sci. Conf., Geochim. Cosmochim. Acta Suppl.*, 5(2), 1097–1117.
- Richardson, J. E. (2009), Cratering saturation and equilibrium: A new model looks at an old problem, *Icarus*, 204, 697–715, doi:10.1016/j.icarus.2009.07.029.
- Richardson, J. E., H. J. Melosh, C. M. Lisse, and B. Carcich (2007), A ballistics analysis of the deep impact ejecta plume: Determining Comet Tempel 1's gravity, mass, and density, *Icarus*, 191(2 Suppl), 176–209, doi:10.1016/j.icarus.2007.08.033.
- Robinson, M. S., et al. (2010), Lunar Reconnaissance Orbiter Camera (LROC) instrument overview, *Space Sci. Rev.*, 150(1–4), 81–124, doi:10.1007/s11214-010-9634-2.
- Russ, P. G., D. S. Burnett, and G. J. Wasserburg (1972), Lunar neutron stratigraphy, *Earth Planet. Sci. Lett.*, 15(2), 172–186, doi:10.1016/0012-821X(72)90058-1.
- Schnetzler, C. C., and J. A. Philpotts (1971), Alkali, alkaline earth, and rare-earth element concentrations in some Apollo 12 soils, rocks, and separated phases, *Proc. 2nd Lunar Sci. Conf.*, 2, 1101–1122.
- Schonfeld, E., and C. J. Meyer (1972), The abundances of components of the lunar soils by a least-squares mixing model and the formation age of KREEP, *Proc. 3rd Lunar Sci. Conf.*, 2, 1397–1420.
- Shoemaker, E. M. (1965), Preliminary analysis of the fine structure of the lunar surface in Mare Cognitum, Ranger VII (Tech. Rep. No. 32-700), 75–134.
- Shoemaker, E. M. (1970), Origin of fragmental debris on the lunar surface and the history of bombardment of the Moon, *Inst. Investig. Geol. la Diput. Prov.*, 25, 27–56.
- Simon, S. B., J. J. Papike, and J. C. Laul (1981), The lunar regolith: Comparative studies of the Apollo and Luna sites. Petrology of soils from Apollo 17, Luna 16, 20, and 24, *Proc. Lunar Planet. Sci. Conf.*, 12B, 371–388.
- Simon, S. B., J. J. Papike, D. C. Gosselin, J. C. Laul, S. S. Hughes, and R. A. Schmitt (1990), Petrology and chemistry of Apollo 17 regolith breccias: A history of mixing of highland and Mare basalt, *Proc. 20th Lunar Planet. Sci. Conf.*, 219–230.
- Solomon, S. C., and J. W. Head (1980), Lunar mascon basins' lava filling, tectonics, and evolution of the lithosphere, *Rev. Geophys.*, 18, 107–141, doi:10.1029/RG018i001p00107g.
- Spudis, P. D., and G. Ryder (1985), Geology and petrology of the Apollo 15 landing site: Past, present, and future understanding, *Eos. Trans. AGU*, 66(43), 721.724–721.726.
- Stoffler, D., G. Ryder, B. A. Ivanov, N. A. Artemieva, M. J. Cintala, and R. A. F. Grieve (2006), Cratering history and lunar chronology, *Rev. Mineral. Geochemistry*, 60(4), 519–596, doi:10.2138/rmg.2006.60.05.
- Swann, G. A., et al. (1972), Preliminary geologic investigation of the Apollo 15 landing site, Apollo 15 Prelim. Sci. Report, NASA SP-289.
- Taylor, S. R. (1982), Planetary science: A lunar perspective, Lunar and Planetary Institute.
- Trombka, J. I., J. R. Arnold, I. Adler, A. E. Metzger, and R. C. Reedy (1974), Lunar elements analysis obtained from the Apollo gamma-ray and X-ray remote sensing experiment, *Proc. Sov. Conf. Cosmochem. MOON PLANETS*.
- Wanke, H., et al. (1972), Multielement analyses of lunar samples and some implications of the results, *Proc. 3rd Lunar Sci. Conf., Suppl.*, 1251–1268.
- Wasson, J. T., and P. A. Baedeker (1972), Provenance of Apollo 12 KREEP, *Proc. 3rd Lunar Sci. Conf.*, 2, 1315–1326.
- Wilhelms, D. E. (1987), The geologic history of the Moon, *U.S. Geol. Surv. Prof. Pap.*, 1348, 283–292.
- Wood, J. A. (1970), Petrology of the lunar soil and geophysical implications, *J. Geophys. Res.*, 75(32), 6497–6513, doi:10.1029/JB075i032p06497.
- Wood, J. A., U. B. Marvin, B. N. Powell, J. Dickey, and J. S. (1970a) *Mineralogy and Petrology of the Apollo 11 Lunar Samples*, vol. 307, Smithsonian Institution, Astrophysical Observatory.

- Wood, J. A., J. S. Dickey, U. B. Marvin, and B. N. Powell (1970b), Lunar anorthosites and a geophysical model of the Moon, *Proceeding Apollo 11 Lunar Sci. Conf.*, 1, 965–988.
- Young, R. A. (1976), The morphological evolution of mare-highland contacts: A potential measure of relative mare surface age, in *Proc. Lunar Sci. Conf. 7th*, pp. 2801–2816, Pergamon Press, New York.
- Zellner, N. E. B., P. D. Spudis, J. W. Delano, and D. C. B. Whittet (2002), Impact glasses from the Apollo 14 landing site and implications for regional geology, *J. Geophys. Res.*, 107(E11), 5102, doi:10.1029/2001JE001800.